



Review Article

Advances in Schottky parameter extraction and applications



Peihua Wangyang ^{a,1}, Xiaolin Huang ^{a,1}, Xiao-Lei Shi ^{b,1}, Niuniu Zhang ^a, Yu Ye ^a, Shuangzhi Zhao ^a, Jiamin Zhang ^a, Yingbo Liu ^a, Fabi Zhang ^a, Xingpeng Liu ^a, Haiou Li ^a, Tangyou Sun ^{a,*}, Ying Peng ^{a,*}, Zhi-Gang Chen ^{b,*}

^a Guangxi Key Laboratory of Precision Navigation Technology and Application, Guilin University of Electronic Technology, Guilin 541004, China

^b School of Chemistry and Physics, ARC Research Hub in Zero-emission Power Generation for Carbon Neutrality, and Centre for Materials Science, Queensland University of Technology, Brisbane, Queensland 4000, Australia

ARTICLE INFO

Article history:

Received 25 April 2024

Revised 24 July 2024

Accepted 27 August 2024

Available online 10 September 2024

Keywords:

Schottky parameter extraction

Photodetectors

Solar cells

Resistive-switching memory

Thin-film transistors

ABSTRACT

Schottky contacts have attracted widespread attention from both the electronic device industry and researchers since their discovery. The Schottky characteristics make these contacts highly suitable for use in field-effect transistors (FETs), photodetectors (PDs), solar cells (SCs), resistive-switching memories (RSMs), thin-film transistors (TFTs), etc. However, how do Schottky contacts affect the device performance? The answer lies simply in the Schottky parameters. This review focuses on the extraction of Schottky parameters, i.e., the Schottky barrier height (SBH), ideality factor (IF), and series resistance (SR), from the current-voltage ($I - V$) curve to understand and analyze the characteristics of Schottky devices. First, the current research progress in this field and the principles of Schottky contacts are presented. Second, this article delves into some classic and widely used extraction methods as well as the latest extraction methods, providing an objective evaluation based on their practical effectiveness. Then, several research applications, including studies that require extraction, simple extraction, and delicate extraction, are enumerated to demonstrate the necessity and importance of Schottky parameter analysis. Finally, an outlook and future research prospects are discussed based on recent progress, and a comprehensive summary is given.

© 2024 Published by Elsevier Ltd on behalf of The editorial office of Journal of Materials Science & Technology.

This is an open access article under the CC BY-NC-ND license (<http://creativecommons.org/licenses/by-nc-nd/4.0/>)

1. Introduction

Metal-semiconductor contacts have emerged as indispensable components in the electronic industry. They have led to great improvements in areas such as high-frequency devices [1–3], solar cells [4–7], solar cell-integrated sensors [8], photodetectors (PDs) [9–11], resistive random-access memories [12–17], thermoelectric devices [18–20], power supplies [21], and high-voltage applications [22]. Due to the uncertainties introduced by the manufacturing process [23,24], the parameters of Schottky diodes significantly vary even when they are fabricated with the same materials. Especially for two-dimensional (2D) devices [25–27], the interface quality and defects significantly affect the device behavior. Therefore, to analyze this behavior, an accurate, reliable procedure for extracting the parameters is urgently needed. However, the ex-

traction procedures proposed by different researchers have their own merits concerning various aspects, which could be confusing. Hence, a systematic review is needed.

Metal-semiconductor (MS) contacts can generally be divided into low-loss ohmic contacts and rectifying Schottky contacts. There is no voltage drop at either end of an MS interface in ohmic contact. In a Schottky contact, a space-charge region is formed on the semiconductor side due to carrier diffusion, so a built-in electric field is formed, which induces a barrier for carriers when they move through the interface. Diodes with Schottky contacts can be modified to meet the needs of high-frequency devices [28–30]. Compared with traditional devices, 2D devices have various interesting features, resulting in competitive performance and advantages such as carrier tunability, and memory effects induced by vertical stacking [31–33]. In practice, the ideality factor (IF) n , Schottky barrier height (SBH) Φ_B and series resistance (SR) R_s are very important for designing and analyzing Schottky devices. Therefore, researchers hope to accurately obtain these characteristic parameters of Schottky diodes from experimental data.

* Corresponding authors.

E-mail addresses: suntangyou@guet.edu.cn (T. Sun), pengying@guet.edu.cn (Y. Peng), zhigang.chen@qut.edu.au (Z.-G. Chen).

¹ These authors contributed equally to this work.

Fortunately, based on the thermionic emission model [34], the current–voltage ($I - V$) characteristics contain information that enables the extraction of these parameters. Many strategies have been proposed to extract the parameters of MS diodes [35,36]. Norde first proposed a straightforward method to extract the value of R_s assuming $n = 1$ (ideal Schottky contact) [37]. In 1985, Lien and Bohlin modified Norde's method to extract the values of n , Φ_B , and R_s from forward $I - V$ curves for $n > 1$ cases [38,39]. Within a year, Cheung and Cheung [40] developed another approach to determine the values of n , Φ_B , and R_s . They found that the n , Φ_B , and R_s of a Schottky diode can be extracted from a single $I - V$ measurement. Additionally, numerical methods have also been well developed. For example, Osvald et al. [41] and Liou et al. [42] proposed vertical and lateral optimization methods, respectively, which minimized the error. Later, extraction procedures for metal–semiconductor–metal (MSM) diodes were also developed after Nouchi established a new model for extracting the parameters of MSM diodes in 2014 [43]. In comparison, the Bennett method is convenient and practical, while Wangyang et al. reported a new approach for extracting n and R_s [44,45]. Although all the methods are somewhat similar, they contain innovative extraction ideas that may have been overlooked.

Our goal is to comprehensively review the advantages and disadvantages of these methods. In this article, we focus on previous works as well as recent advances to find connections and improvements. First, MS contact theory is thoroughly described. Then, we briefly outline the appeal of each method, followed by objective comments on the merits and limitations. The practical applications of these methods are assessed to clarify for readers if a method is applicable. Finally, a summary is given regarding improvements that have been made and potential challenges in the future.

2. Classical theory

The energy band diagram showing the formation of a Schottky barrier is displayed in Fig. 1(a) (e.g., n-type). If the metal and semiconductor are properly connected, then due to the different work functions, carriers drift from the semiconductor into the metal, and the two Fermi levels are forced to align in this case, as shown in Fig. 1(b). As a result, a space-charge region is formed, which causes the band to bend. As a result, a barrier is induced, and the height of the barrier is determined by:

$$\Phi_B = \Phi_m - \chi_s \quad (1)$$

For practical MS contacts, the ideal situation, as shown in Fig. 1(c), is never reached because of the presence of a 10–20 Å thick insulating layer of oxide at the interface [34]. The oxide layer is usually so thin that electrons can easily tunnel through it, and Fig. 1(b, c) is nearly identical with respect to electrons.

In most cases, the SBH is greater than kT/q (some studies may define it as V_T) at room temperature, but some electrons may absorb enough energy to overcome the barrier. This process is called “thermionic emission” (TE). An electron can travel through the barrier in other ways, such as via “field emission” (FE) and “thermionic-field emission” (TFE). In this article, we mainly discuss extraction methods based on the TE model.

2.1. Single Schottky diodes

2.1.1. Thermionic model

When a forward bias V_D is applied to the device, the barrier that carriers must overcome to travel from the semiconductor into the metal is equal to $\Phi_B - V_D$. This carrier movement forms a current from the metal to the semiconductor. The current density can be described by [46]:

$$J_{\text{forward}} = A^* T^2 \exp[-q(\Phi_B - V_D)/kT] \quad (2)$$

where A^* is the Richardson constant. Generally, the barrier does not change with the bias, making $J_{\text{forward}}|_{V_D=0}$ a constant, and it is equal to $-J_{\text{reverse}}$ due to the thermal equilibrium condition. In other words, when $V_D = 0$, the magnitudes of J_{forward} and J_{reverse} are equal, and their directions are opposite, which gives:

$$J_{\text{reverse}} = -J_{\text{forward}}|_{V_D=0} = -A^* T^2 \exp[-q(\Phi_B)/kT] \quad (3)$$

From Eqs. (2) and (3), we can deduce that the total current density is:

$$J = J_{\text{forward}} + J_{\text{reverse}} = J_{\text{st}} [\exp(qV_D/kT) - 1] \quad (4)$$

$$J_{\text{st}} = A^* T^2 \exp[-q(\Phi_B)/kT] \quad (5)$$

where J_{st} is considered the saturation current. If it is known, then we can deduce Φ_B from:

$$\Phi_B = \frac{kT}{q} \ln \frac{A^* T^2}{J_{\text{st}}} \quad (6)$$

Eq. (6) presents the general idea for calculating the Φ_B of an ideal Schottky diode. However, Eq. (4) cannot explain measured $I - V$ curves, which do not fit well with theoretical synthetic data.

2.1.2. Image-force-lowering modification

If the barrier height remains constant regardless of the bias, then Eq. (4) derived from TE theory predicts $I - V$ characteristics that resemble the ideal rectifier characteristics. However, as observed in practical cases [47], the SBH may depend on the electric field in the space-charge region and hence on the applied bias. In fact, the barrier height is reduced by $\Delta\Phi_i$ due to the image force, which depends on the bias. The effective barrier height can therefore be written as:

$$\Phi_B = \Phi_{B0} - \Delta\Phi_i \quad (7)$$

This bias is the dependence of Φ_B modifies the $I - V$ characteristics.

Suppose that $d\Phi_B/dV$ is a constant, based on which we can rewrite Eq. (7) as follows:

$$\Phi'_B = \Phi_{B0} - \Delta\Phi_i + \alpha V_D \quad (8)$$

where α refers to $d\Phi_B/dV$. The coefficient α must be positive because Φ_B always increases with increasing forward bias. The current density now becomes:

$$\begin{aligned} J &= A^* T^2 \exp\left[-\frac{q(\Phi_{B0} - \Delta\Phi_i + \alpha V_D)}{kT}\right] \left[\exp\left(\frac{qV_D}{kT}\right) - 1\right] \\ &= J_{\text{st}} \exp\left[-\alpha qV_D/kT\right] \left[\exp\left(\frac{qV_D}{kT}\right) - 1\right] \end{aligned} \quad (9)$$

where $J_{\text{st}} = A^* T^2 \exp[-q\Phi_{B0}/kT]$. Rearranging Eq. (9) and setting $\frac{1}{n} = 1 - \alpha$, this equation becomes:

$$J = J_{\text{st}} \exp\left(\frac{qV_D}{nkT}\right) \left[1 - \exp\left(-\frac{qV_D}{kT}\right)\right] \quad (10)$$

where n is called the IF, and its value can be calculated from the plot of $\log[J/(1 - \exp(-qV_D/kT))]$ versus V_D . This plot is linear down to zero, as shown in Fig. 1(d), with a slope of q/nkT if n is constant, even for $V < 3kT/q$ and for a reverse bias [46,48].

In most cases, $\alpha = d\Phi_B/dV_D$ is not a constant, and the plot of $\log[J/(1 - \exp(-qV_D/kT))]$ versus V_D is not linear. Consequently, the IF defined by $\frac{1}{n} = 1 - \alpha$ is now a function of V_D , but the use of the plot (Fig. 1(d)) is still a very practical idea, and the IF can be obtained from the experimental $I - V$ curves through Eq. (10). In studies [49], this curve is usually linear over a certain range, whereas the curve deviates from the expected straight line outside this range. The deviation from linearity is usually due to the SR and IF.

Commonly, the IF represents not only the image-force-lowering effect but also other factors that cause deviations from the ideal Schottky contact behavior, such as interfacial states [50], tunneling effects [51], and recombination currents [52].

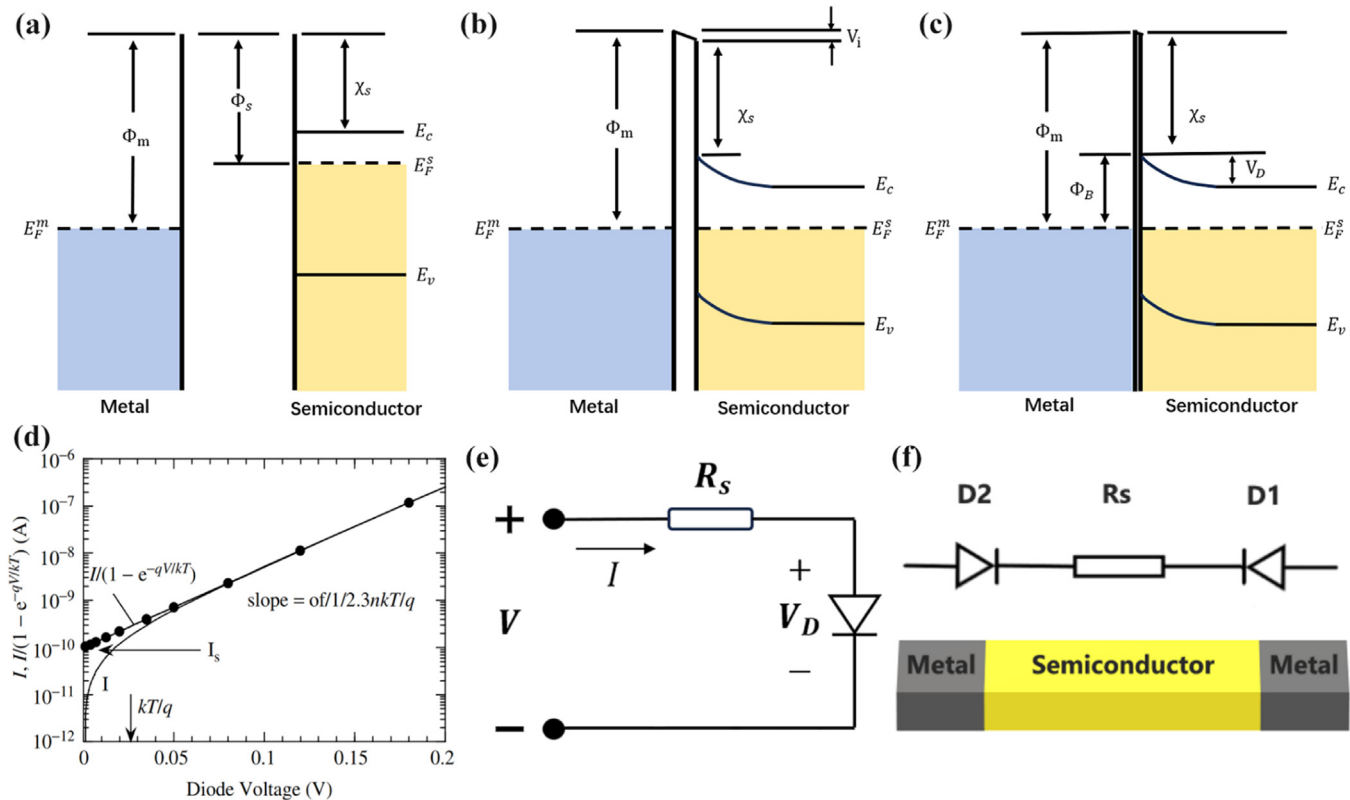


Fig. 1. (a) Band diagrams of metal-semiconductor contact. (d) I – V curve of a Schottky diode and $\log J/[1 - \exp(-qV_0/nkT)]$ as the y -axis. Reproduced with permission [46]. Copyright 2006, John Wiley&Sons. (e) A single diode's equivalent circuit. (f) Double-sided asymmetric Schottky Diode and its equivalent circuit.

2.1.3. Series resistance modification

The equivalent circuit in Fig. 1(e) can represent an MS diode consisting of an ideal diode in series with a resistance R_s . When current flows through the device, the diode voltage V can be considered the sum of the voltage drops at the junction and the SR (V_D and IR_s , respectively):

$$V = V_D + IR_s \quad (11)$$

Then, Eq. (4) becomes:

$$I = AJ = AJ_{st} \left[\exp \frac{q(V - IR_s)}{kT} - 1 \right] \quad (12)$$

where A is the contact area and Eq. (12) describes the total current of the diode. By substituting Eqs. (11) into (10), we obtain a new form of the I – V characteristics:

$$I = AJ = AJ_{st} \exp \left(\frac{q(V - IR_s)}{nkT} \right) \left[1 - \exp \left(\frac{-q(V - IR_s)}{kT} \right) \right] \approx AJ_{st} \left[\exp \frac{q(V - IR_s)}{nkT} - 1 \right] \quad (13a)$$

or in its voltage form:

$$V = \frac{nKT}{q} \ln \left(\frac{I}{J_{st}} + 1 \right) + IR_s \quad (13b)$$

This form is relatively correct, and we can extract both n and R_s from the measured I – V characteristics.

2.2. Back-to-back Schottky diodes

When a device is processed such that metal is deposited on each side of the semiconductor, an MSM structure is obtained. This structure has unique characteristics: the SR can be seen as a single equivalent resistance, and the two contacts are constrained by

each other. From this, we can deduce the following fascinating relationships:

$$J = J_1 = -J_2 \quad (14)$$

$$V = |V_{D1}| + |V_{D2}| + IR_s \quad (15)$$

Assuming that an n-type semiconductor has metal electrodes deposited at both ends, as shown in Fig. 1(f), a Schottky barrier will be formed on both sides of the semiconductor; thus, this structure can be seen as two asymmetric Schottky diodes connected by an SR between them. Luckily, the same model discussed in Section 2.1 can be applied to this asymmetric structure. Eq. (12) can be expressed as follows:

$$J = J_{st} \left[\exp \left(\frac{qV_D}{nkT} \right) - 1 \right] \quad (16)$$

From Eqs. (14)–(16), assuming that $|V_{D1}| = |V_{D2}| = (V - IR_s)/2$, one can express the I – V characteristics of two asymmetric Schottky diodes as follows [53]:

$$J = \frac{2J_{st1}J_{st2} \sinh \left[\frac{q(V - IR_s)}{2nkT} \right]}{J_{st1} \exp \left[\frac{-q(V - IR_s)}{2nkT} \right] + J_{st2} \exp \left[\frac{q(V - IR_s)}{2nkT} \right]} \quad (17)$$

where J_{st1} and J_{st2} are the saturation currents of D1 and D2, respectively. When a bias V is applied to one side while the other side is grounded, we can infer that one diode is under a forward bias while the other is the opposite regardless of whether the bias V is positive. Eq. (17) has been used in analyzing back-to-back Schottky diodes with good coherence between the experiment and theoretical model [54]. Furthermore, Eq. (17) can be used to recover the I – V characteristics of a single Schottky contact by assuming

that one of the barriers is zero. This Schottky diode model also enables easy extraction of the diode parameters, which we will discuss later.

3. Extraction methods

To see how these extraction methods are developed, we present the existing methods chronologically in two different structures – Single-sided and back-to-back Schottky diodes. These methods are all based on the thermionic model but are achieved differently.

3.1. Single Schottky diodes

As we have discussed above, Schottky diode parameters can be extracted using the traditional method by plotting $\ln J/[1 - \exp(\frac{qV}{kT})]$ versus V . With the slope q/nkT and intercept of $\ln J_{st}$, one can easily obtain the values of n and Φ_B by simply calculating Eq. (5). However, this method is incorrect when the voltage across R_s cannot be ignored, so researchers proposed alternative methods.

3.1.1. Norde–High series resistance [37]

Considerable attention has been given to the nonlinear effects of Schottky contacts. Norde was the first to propose a parameter extraction method for correcting the nonlinearities induced by a large R_s [37].

In the traditional (or ideal) approach, a logarithmic plot that linearizes the $I - V$ characteristics is introduced. However, in practice, the linear region in this plot is often limited to $kT/q \ll V \ll IR_s$. Furthermore, the generation-recombination current contributes a significant portion of the total current at low bias voltages. Norde proposed a function to overcome these limits by introducing the following function:

$$F(V) = \frac{V}{2} - \frac{kT}{q} \ln \left(\frac{I}{AA^*T^2} \right) \quad (18)$$

Assuming that $kT/q \ll V$, Eqs. (4) and (18) yield:

$$F(V) = \Phi_B + IR_s - \frac{V}{2} \quad (19)$$

Differentiating Eqs. (19) and (12) with respect to V and combining these two equations gives:

$$\frac{dF}{dV} = -\frac{1}{2} + \frac{\beta IR_s}{1 + \beta IR_s} \quad (20)$$

where $\beta = q/kT$. From Eq. (20), we can deduce the current I_0 at the minimum value by setting $dF/dV = 0$; we obtain $I_0 = kT/qR_s$, and with Eq. (12), $V_0 = kT/q + \ln(\frac{I_0}{AA^*T^2})$. Hence, the value of Φ_B is given by:

$$\Phi_B = F(V_0) + \frac{V_0}{2} - \frac{kT}{q} \quad (21)$$

The experimental $F(V)$ plots of different Schottky diodes are shown in Fig. 2(a). The extracted value of Φ_B is in accordance with the expected value.

This method using forward $I - V$ characteristics provides insights into the SR and the SBH that are completely different from those obtained with the traditional approach for the first time, has innovative significance, and establishes a foundation for studying a new method of extracting Schottky diode parameters through forward $I - V$ characteristics [55].

Norde's method has been widely used and verified in multiple studies [56,57] showing that it can be adapted to study the characteristics of Schottky diodes. By plotting several Norde plots, Korucu et al. [58] confirmed that the SR is almost independent of temperature.

Table 1

Values of R_s and SBH of Au/(Cu₂O-CuO-PVA)/n-Si Schottky diode extracted from modified Norde's function. Reproduced with permission [62].

T (K)	Φ_{b0} ($I - V$ method) (eV)	Φ_{b0} (Norde) (eV)	R_s (kΩ)
100	0.27	0.30	1064.99
120	0.33	0.35	384.30
160	0.44	0.47	95.64
200	0.57	0.61	6.98
240	0.66	0.70	3.30
280	0.76	0.80	2.78
300	0.81	0.83	1.12
320	0.87	0.86	0.61
340	0.93	0.93	0.28
360	0.97	1.00	0.17
380	0.99	1.04	0.03

However, according to Aubry and Meyer [35], inaccuracies exist when only the minimum value of $F(V)$ is taken to determine the parameters. Moreover, issues may arise when various factors, such as temperature, humidity, and density, affect the manufacturing process, making the IF not always unity, as expected. Sato and Yasumura [59] improved this method by using two $F(V, I)$ values obtained at different temperatures (129 and 297 K). They proposed that Φ_B , n , and R_s can be determined even if $1 < n < 2$. They also proved that n is temperature dependent [59–61]. Below, generalized Norde's plot approaches are presented.

3.1.2. Lien, Bolin–Generalized Norde's plot [38,39]

To eliminate the two problems mentioned above, i.e., (1) the IF is not always unity and (2) statistical errors exist due to insufficient data points, Lien et al. [38] suggested two methods for obtaining R_s and using it to plot $\ln I$ versus V . The standard $I - V$ method is then applied to extract n and Φ_B . In the first method, R_s is obtained by plotting several Norde functions versus I :

$$F_a(V) = \frac{V}{a} - \frac{kT}{q} \ln \left(\frac{I}{AA^*T^2} \right) \quad (22)$$

Assuming that $F_a(V)$ has a minimum value when $dF_a/I = 0$ (assuming that this occurs at $I = I_a$), with Equation $I = I_{st} \exp(\frac{qV_D}{nkT})$ ($V_D \gg kT/q$), one can deduce the following [38]:

$$I_a = \frac{(a - n)kT}{R_s q} \quad (23)$$

This equation indicates that I_a versus a is a straight line (as shown in Fig. 2(b)), and the value of R_s can be determined from the slope of this line, while the intercept at $a = 0$ gives the value of n . Once the contribution of R_s to the experimental data points is subtracted, the curve described by $I = I_{st} \exp(\frac{qV_D}{nkT})$ is fitted to the measured data, and the precise values of Φ_B and n are determined.

The advantage of using several different values of a lies in making use of an extra range of the $I - V$ characteristics to achieve better accuracy [38]. Bohlin proposed the generalized Norde plot, which allows the determination of Φ_B , R_s , and n with only one $I - V$ measurement at a specific temperature [39]. According to Ulu-san et al. [62], the SBH values of Au/(Cu₂O-CuO-PVA)/n-Si Schottky diodes obtained from $\ln I - V$ and the Bohlin-modified Norde's function are consistent (as shown in Table 1), which shows the accuracy and feasibility of the approach.

Compared to the method proposed by Lien et al. [38], the Bohlin method can be used to monitor deviations from ideal conditions. However, Bohlin used only two values of a , corresponding to two experimental data points, resulting in lower accuracy [38,39].

This method is accurate under the condition $V_D > 3kT/q$, and there is an opportunity for it to function under higher R_s by increasing the value of a . Fig. 2(c) shows that a must be greater than

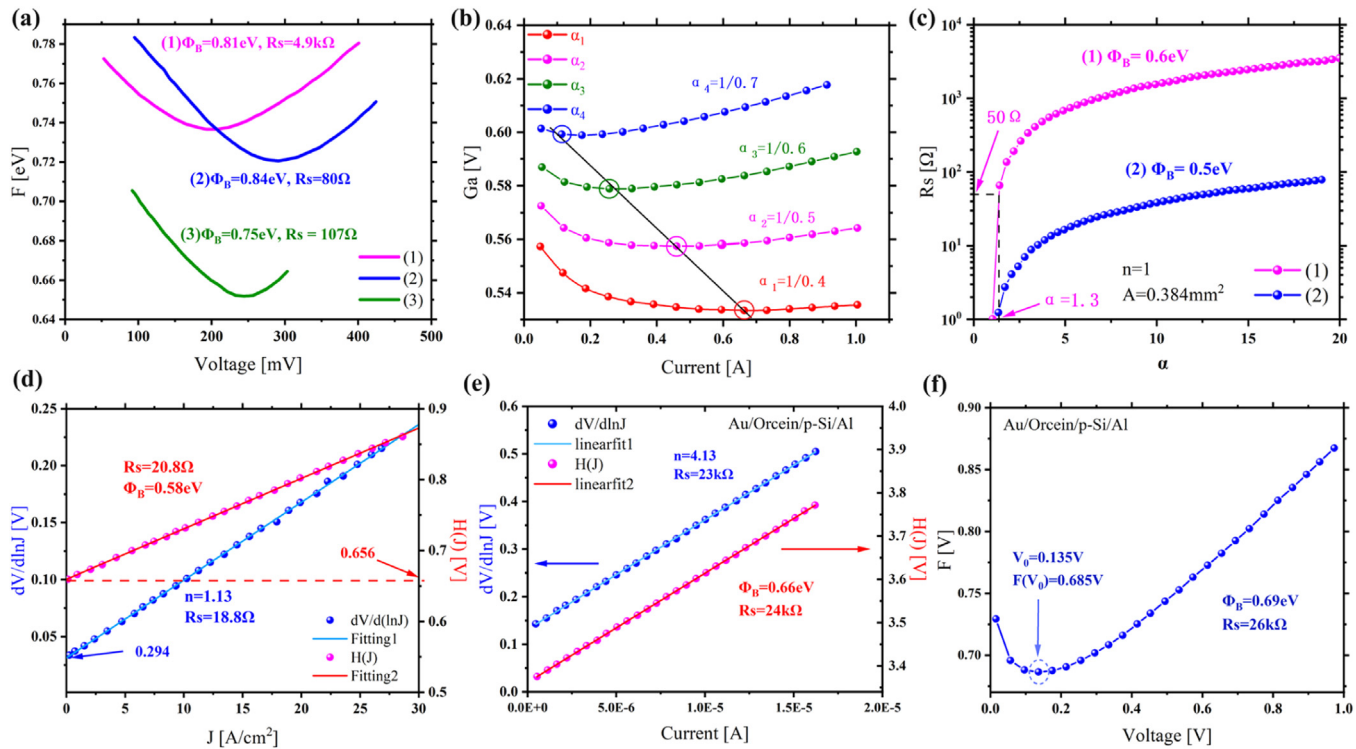


Fig. 2. (a) Experimental plots of $F(V)$ for three different Schottky diodes: (1) Au on CP6-etched n-Si. (2) Pt-Si on n-Si. (3) Pd-Si on n-Si. Reproduced with permission [37]. Copyright 2008, Springer. (b) Recalculated $G_a(I)$ with different a calculated from measured I-V data. For each a , $G_a(I)$ has a minimum at $I = I_a$ [38]. (c) R_s versus a to satisfy the condition for the Lien et al.'s method [38]. Reproduced with permission [35]. Copyright 1994, Springer. (d) A Plot of $dV/d(\ln J)$ versus J and $H(J)$ versus I of as-deposited W/GaAs Schottky diode. Reproduced with permission [40]. Copyright 1986, Springer. (e) A plot of $dV/d(\ln I)$ versus I and $H(J)$ versus I obtained from forward bias $I - V$ characteristics of the Au/Orcein/p-Si/Al structure. Reproduced with permission [64]. Copyright 2010, Springer. (f) $F(V)$ versus V plot of the Au/Orcein/p-Si/Al structure. Reproduced with permission [64]. Copyright 2010, Springer.

1.3 when $R_s = 50$. Theoretically, a can be increased up to a certain value to improve the accuracy. This value corresponds to the maximum power that can be applied to the diode. However, if the voltage drops across R_s is greater than V_D , then the effect on the $I - V$ characteristics is too strong to accurately extract the Schottky parameters. Consequently, the value of a is limited [35].

3.1.3. S.K. Cheung's method— R_s double check [40]

Cheung's method [40] provides another way of extracting the Schottky contact parameters. According to Eq. (13b), the voltage is also expressed as:

$$V = AJR_s + n\Phi_B + \frac{nKT}{q} \ln \left(\frac{J}{A^*T^2} \right) \quad (24)$$

By differentiating Eq. (24) and rearranging terms, we obtain:

$$\frac{dV}{d(\ln J)} = AJR_s + \frac{nKT}{q} \quad (25)$$

Eq. (25) yields a straight line with a slope of R_sA and an intercept of nKT/q . By linear fitting Eq. (25), one can easily extract the value of R_s and n . Another linear plot with a slope of R_sA is obtained when plotting $dV/d(\ln J)$ versus J . To extract Φ_B , Cheung rearranged Eq. (24) and defined the function $H(J) = V - \frac{nKT}{q} \ln \left(\frac{J}{A^*T^2} \right)$, which gives:

$$H(J) = AJR_s + n\Phi_B \quad (26)$$

The plot of $H(J)$ is also a straight line with an intercept of $n\Phi_B$. By fitting Eqs. (25) and (26) to experimental data, the values of n , Φ_B , and R_s can be obtained. The slope of this plot also yields the value of R_s . Both Eqs. (25) and (26) give the value of R_s . Eq. (25) is the first derivative of Eqs. (24), and Eq. (26) is the variant of Eq. (24), thus there should exist a consistency between

Eqs. (25) and (26) theoretically. Hence by comparing the two values of R_s , one can verify the consistency of the method. In other words, if consistency exists, the results are reliable to some extent. As shown in Fig. 2(d), the R_s values extracted from two different plots agree with each other within 10 %. n and Φ_B also correspond with the reported $\ln J$ vs. V plot [63].

According to Sakir (data shown in Fig. 2(e, f)), the values of R_s obtained from the $H(J) - I$ curve are close to the values obtained from the $dV/d(\ln I) - I$ plot and the values of all the parameters extracted by the different approaches agree well with each other [64]. This method improves upon the techniques used by Norde [37] as well as Sato and Yasumura [59]. Compared to the former, it eliminates the need to find the minimum value of the Norde function, thus avoiding potential errors due to minor data points. Compared to the latter, only a single $I - V$ measurement is required to obtain the Schottky diode parameters. Additionally, S.K. and Cheung et al.'s [40] procedure allows convenient calculation of R_s , Φ_B , and n through a single $I - V$ measurement [65–67]. However, this method may not accurately determine the Φ_B of certain heterostructure field-effect transistors (HFETs) [68]. Moreover, the presence of voltage drops across the interface layer and bias-dependent effects on the interface states can lead to uncertainties in the n obtained from the downward curvature region in the forward $I - V$ curve compared to the linear region with similar characteristics [69].

3.1.4. Werner's method—Shunt resistance [70]

Werner proposed three different plots to extract Φ_B , n , and R_s , avoiding Norde's functions that use the small-signal conductance model [70]. This method has since been used in various studies, including for PDs and solar cells [71,72].

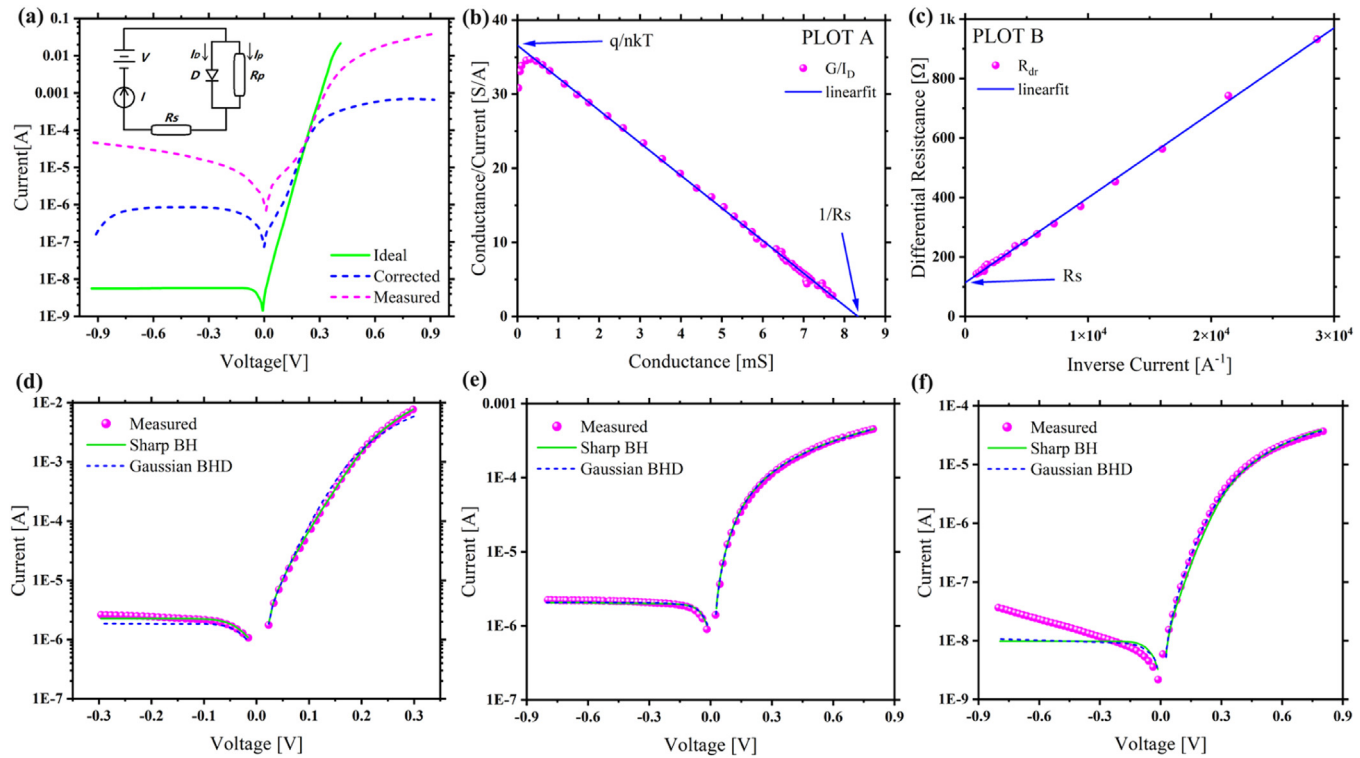


Fig. 3. (a) Current/voltage curves of a PtSi/Si diode. Insert shows the equivalent circuit with series resistance R_s shunt resistance R_p . Reproduced with permission [70]. Copyright 1988, Springer. (b) Plot A yields R_s and n from the X and Y-intercepts. Reproduced with permission [70]. Copyright 1988, Springer. (c) Plot B yields R_s from the Y-intercept and n from the slope. Reproduced with permission [70]. Copyright 1988, Springer. (d–f) I – V curves of (d) Hg/n-Si(111)1 × 1-H, (e) Pb/n-Si(111)1 × 1-H, (f) Pb/p-Si(111)1 × 1-H Schottky diodes and comparison between the experimental data, the sharp barrier height fit, and the fit with the Gaussian BHD. Reproduced with permission [41]. Copyright 1996, IOP Publishing.

The three plots (A, B, and C) are all based on inducing the shunt conductance G_p (shown in the inset of Fig. 3(a)), which is derived from the reverse characteristics. In this model, the current I is expressed as:

$$I = I_D + I_p = I_{st} \left[\exp\left(\frac{q(V - IR_s)}{nkT}\right) - 1 \right] + G_p(V - IR_s) \quad (27)$$

Here, I_D is the current through the diode, and I_p is the shunt current with resistance $R_p = 1/G_p$, which is related to edge effects and volume recombination [70]. Differentiating I_D yields small-signal conductance $G = \frac{dI_D}{dV}$, and:

$$\frac{G}{I_D} = \frac{q}{nkT} (1 - GR_s) \quad (28)$$

Eq. (28) shows that a plot of G/I_D versus G (termed plot A) yields a straight line with a y -axis intercept of q/nkT , an x -axis intercept of $1/R_s$ and slope $-qR_s/nkT$. From Eq. (28), assuming that $1/G = R_{dr}$, which is the differential resistance of the I – V curve:

$$R_{dr} = \frac{nkt}{qI_D} + R_s \quad (29)$$

Using correlation, Eq. (25) was obtained in its current form:

$$\frac{dV}{d(\ln I_D)} = I_D R_s + \frac{nkt}{q} \quad (30)$$

Eq. (29) provides insight into the behavior of the differential resistance R_{dr} , as it is related to the inverse current $1/I_D$ characterized by a slope of nkt/q and a y -axis intercept of R_s (termed plot B). Eq. (30) was used by Cheung and Cheung as we previously discussed, and we do not further elaborate [40]. Plot A shown in Fig. 3(b) demonstrates the impact of the generation-recombination current through G_p , which does not substantially contribute to R_s . The use of G_p seems to be the most sensitive way to demonstrate the contribution of this mechanism to the overall current [35]. Plots A and B yield R_s and n with good consistency,

as shown in Fig. 3(b, c), with plot A yielding $R_s = 120 \Omega$ and $n = 1.08$, plot B yielding $R_s = 119 \Omega$ and $n = 1.11$, and plot C yielding $R_s = 120 \Omega$ and $n = 1.09$ (not shown).

According to Meyer's group [35], these values must be obtained from the linear section of plot A, where the Schottky parameters can be effectively and accurately determined. If there are several data points at low voltages, then due to electrical noise, random scattering, the shunt current, or incomplete correction of the shunt current, these data points may alter the slope and y -intercept of the fitting, resulting in an unreliable value for the corresponding SR [55].

Nonetheless, Werner's method is very applicable but inconvenient compared to Cheung's method [40,73]. This is probably due to the unreliable numerical determination of G_p , which usually requires voltage steps of <1 mV to derive an accurate slope of $G = dI_D/dV$. In some solar cell cases, plot A does not yield a straight line, as suggested by Werner [74].

Additionally, plotting so many curves may raise uncertainties, especially among graphical approaches [75]. Chattopadhyay's model [76] has been suggested to be suitable for determining R_s from forward I – V curves and high-frequency C – V curves.

3.1.5. Error-minimization extraction methods

Osvald's method—Vertical error minimization [41]

The methods discussed above are all based on plotting variants of the I – V characteristics. However, limitations arise because of the linearity requirement, which becomes noticeable when the influence of the SR dominates in small devices. All of these approaches completely exclude reverse bias experimental data when extracting the parameters. For such cases, more complex methods must be employed.

To utilize the entire bias range of the characteristics for parameter extraction, Osvald et al. [41] applied least squares for maximum likelihood estimation and described the sum of the squares as follows:

$$S = \sum_{i=1}^N \left(\frac{I_{ei} - I_i}{I_i} \right)^2 \quad (31)$$

where I_{ei} is the i th experimental value, I_i is the current fitting value, and N is the number of measuring points. Eq. (31) implies that all the points of the $I-V$ curve are measured with the same relative error. Notably, the notion of SBH inhomogeneities has garnered considerable recognition, with extensive documentation elucidating their impact on electrical properties [47,77]. Therefore, different diodes with homogeneous and inhomogeneous forms are both worth studying.

Homogeneous diodes: By minimizing the sum of the errors, non-linear equations that are solved by iterative methods (e.g. simplified Newton-Raphson method) are obtained [78].

$$\frac{\partial S}{\partial \Phi_B} \approx \sum_{i=1}^N \left(\frac{I_{ei}}{I_i} - 1 \right) \frac{I_{ei}}{I_i} \frac{1}{n + \beta R_s(I_i + I_s)} = 0$$

$$\frac{\partial S}{\partial n} \approx \sum_{i=1}^N \left(\frac{I_{ei}}{I_i} - 1 \right) \frac{I_{ei}}{I_i} \frac{(I_i + I_s)(V_i/I_i - R_s)}{n + \beta R_s(I_i + I_s)} = 0$$

$$\frac{\partial S}{\partial R_s} \approx \sum_{i=1}^N \left(\frac{I_{ei}}{I_i} - 1 \right) \frac{I_{ei}}{I_i} \frac{(I_i + I_s)}{n + \beta R_s(I_i + I_s)} = 0$$

These equations can be used to extract parameters Φ_B , n , and R_s from the $I-V$ curve not only for pure TE but also for a combination of two other current conduction mechanisms.

Inhomogeneous diodes: The inhomogeneity of SBH was often incorporated into the IF, but Osvald and Dobrocka [41] suggest that it is insufficient. Hence they induced a concept—Barrier Height Distribution (BHD). Though the BHD is not directly accessible by a single experiment, it can be reconstructed from a large database by statistical methods [41]. Based on the analysis of published papers, Osvald finds that a Gaussian distribution would be appropriate for describing the BHD. The simplified description of an inhomogeneous system can be described by: the mean value of the BHD Φ_{B0} , standard deviation σ and an SR of the unit area $r = R_s/A$. Define Gaussian BHD $\rho(\Phi_B; \Phi_{B0}, \sigma) = \frac{1}{\sqrt{2\pi}\sigma} \exp(-\frac{(\Phi_B - \Phi_{B0})^2}{2\sigma^2})$ and current density J from Eq. (12) only replace the R_s with r , then the total current of the diode can be expressed as:

$$I(\Phi_{B0}, \sigma, r) = A \int \rho(\Phi_B; \Phi_{B0}, \sigma) J(\Phi_B; r) d\Phi_B \quad (32)$$

Similarly, a minimum error is required:

$$\frac{\partial S}{\partial \Phi_{B0}} \approx \sum_{i=1}^N \left(\frac{I_{ei}}{I_i} - 1 \right) \frac{I_{ei}}{I_i^2} \int \frac{\Phi_B - \Phi_{B0}}{\sigma^2} \rho J_i d\Phi_B = 0$$

$$\frac{\partial S}{\partial \sigma} \approx \sum_{i=1}^N \left(\frac{I_{ei}}{I_i} - 1 \right) \frac{I_{ei}}{I_i^2} \int \frac{(\Phi_B - \Phi_{B0})^2 - \sigma^2}{\sigma^3} \rho J_i d\Phi_B = 0$$

$$\frac{\partial S}{\partial r} \approx \sum_{i=1}^N \left(\frac{I_{ei}}{I_i} - 1 \right) \frac{I_{ei}}{I_i^2} \int \frac{J_i + J_s}{1 + \beta r(J_i + J_s)} \rho J_i d\Phi_B = 0$$

The solutions can again be found via iterative method using MATLAB software by MathWorks, Inc.®. This approach explains the electrical characteristics of Schottky diodes without using n and is therefore ambiguous.

As shown in Fig. 3(d, e), the inhomogeneous diode concept can be used to explain the behavior only when TE is the only transport mechanism, thus resulting in poor agreement between the

experimental and simulated curves [79]. The non-saturated reverse (Fig. 3(f)) current cannot be explained without considering voltage modification of the barrier height profile. This method enables the extraction of the SBH even with high resistance and bypasses the need for a linear part of the $\ln I$ versus V plot [41].

Because Osvald's methods are computationally intensive, they require powerful software and computers. Fortunately, the concept is simple enough, and computational tools are progressing; hence, the methods are very useful and applicable [42].

Liou's method—lateral error optimization [42]

Different from Osvald's emphasis on vertical error adjustment [41], Liou's group [42] focused more on a lesser-known yet powerful method of lateral error adjustment. Using Eq. (13b), one can simulate a voltage for a specific given current. By minimizing the errors in the voltage, the sum of the lateral quadratic error is:

$$S_L = \sum_{i=1}^N \left(\frac{V_{ei} - V_i}{V_i} \right)^2 \quad (33)$$

where N is the number of data points, V_{ei} is the experimental voltage, and V_i is the simulated voltage. V_i are simulated voltages that are associated with three parameters— Φ_B , n , and R_s , and it can be directly calculated from the $I-V$ relationship described by Eq. (13b), while for vertical optimization, an iterative solution is needed. Eq. (33) is employed to minimize the lateral error, which is related to the simulated voltage. With the models described by Eqs. (13b) and (33) inputted, one can easily use the tool 'nlregb' incorporated in S-PLUS statistical computing software to extract the value of Φ_B , n , and R_s that corepond to the minimum S_L .

For comparison, Liou [42] used the 'Advanced Interconnect Modeling Simulation Program with Integrated Circuit Emphasis (SPICE)' to generate both simulated and measured data. The measured data containing possible errors are expressed as:

$$I_{\text{with noise}} = I_{\text{noise-free}} * (1 + \gamma Q) \quad (34)$$

where $I_{\text{noise-free}}$ is the simulated current, $I_{\text{with noise}}$ is the current used in parameter extraction, γ is the relative percentage of the error to be added and Q is a randomly generated number within -1 to +1.

This approach offers the benefit of being able to determine whether a method has converged to the global optimum and to determine the parameters most influenced by the noise level [80]. The relative errors in R_s , n , and I_s are reported to be very small for the extracted parameters when the noise level is <20 %, while the errors become questionable otherwise due to the high noise level or when the resistance approaches 1 MΩ [42]. According to Liou, both the lateral and vertical optimizations are equally insensitive to measurement errors; thus, they have the same degree of robustness and accuracy [42]. However, lateral optimization is much more efficient than vertical optimization, although both methods require an appropriate choice of the initial values; otherwise, non-convergence may occur even when a high computational load is utilized [42,81].

Additionally, both methods utilize the entire range of the $I-V$ curves to simultaneously extract the parameters, which is straightforward and has gained popularity. Nevertheless, they do not take the effect of the shunt resistance into account [82].

3.1.6. Aazou's methods—Extraction based on the Lambertw function solution [82]

Aazou et al. [82] recently proposed approaches that do not require very high computational resources while covering the entire voltage range. They proposed 3 different methods. The initial approach involves the utilization of the analytical formula of dynamic conductance. The second approach relies on the integration of the current analytical expression. Finally, the final method makes use of a dedicated function within the Mathematica software.

The LambertW function: According to Aazou et al. [82], Eq. (27) is a transcendental equation that implicitly relates the current and the voltage. To make it much more compact, they defined:

$$w * \exp(w) = x \quad (35)$$

where

$$w = \frac{-q(V - IR_s)}{nkT} + \frac{q(R_s I_s + V)}{nkT(1 + G_p R_s)}$$

$$x = \frac{qR_s I_s}{nkT(1 + G_p R_s)} \exp\left(\frac{q(R_s I_s + V)}{nkT(1 + G_p R_s)}\right)$$

The solution $w(x)$ to Eq. (35) is given by the multi-valued Lambert W function [83], denoted as $LambertW_k(x)$. As proposed by Aazou, the appropriate branch of the Lambert W function is $k = 0$, which meets the condition $LambertW_0(x) = 0$ when $x = 0$. Thus, the solution $w(x)$ to Eq. (35) can be expressed as [82]:

$$w = LambertW_0(x)$$

which is

$$\begin{aligned} & \frac{-q(V - IR_s)}{nkT} + \frac{q(R_s I_s + V)}{nkT(1 + G_p R_s)} \\ &= LambertW\left[\frac{qR_s I_s}{nkT(1 + G_p R_s)} \exp\left(\frac{q(R_s I_s + V)}{nkT(1 + G_p R_s)}\right)\right] \end{aligned} \quad (36)$$

By rewriting Eq. (36) in the form of explicit expression, and denoting $LambertW$ as W the current is given by [82]:

$$I = \frac{nkT}{qR_s} W\left[\frac{qR_s I_s}{nkT(1 + G_p R_s)} \exp\left(\frac{q(R_s I_s + V)}{nkT(1 + G_p R_s)}\right)\right] - \frac{I_s - V G_p}{1 + G_p R_s} \quad (37)$$

The inverse function explicitly expresses the voltage as follows:

$$V = -\frac{nkT}{q} W\left[\frac{qI}{nkT G_p} \exp\left(\frac{q(I + I_s)}{nkT G_p}\right)\right] + I\left(R_s + \frac{1}{G_p}\right) \quad (38)$$

Dynamic Conductance: The dynamic conductance method relies on fitting experimental data to an analytical expression obtained from Eq. (38). Define:

$$a_1 = \frac{qR_s I_s}{nkT(1 + G_p R_s)}, \quad a_2 = R_s I_s, \quad a_3 = \frac{nkT(1 + G_p R_s)}{q},$$

$$a_4 = \frac{nkT}{qR_s}, \quad a_5 = -\frac{I_s}{1 + G_p R_s}, \quad a_6 = \frac{G_p}{1 + G_p R_s}$$

Then Eq. (38) becomes:

$$I = a_4 W\left[a_1 \exp\left(\frac{V+a_2}{a_3}\right)\right] + a_6 V + a_5 \quad (39)$$

Taking the derivative of Eq. (39) with respect to V and rearranging it results in an equation that expresses the voltage as a function of the dynamic conductance, current, voltage, and parameters:

$$V = \alpha_G \frac{dI}{dV} + \alpha_{IG} I \frac{dI}{dV} + \alpha_{VG} V \frac{dI}{dV} + \alpha_I I + \alpha_0 \quad (40)$$

where the coefficients are:

$$\alpha_G = -\frac{nkT(1 + R_s)}{qG_p} - \frac{R_s I_s}{G_p}, \quad \alpha_{IG} = -\frac{R_s(1 + G_p R_s)}{G_p},$$

$$\alpha_{VG} = R_s, \quad \alpha_I = R_s + \frac{1}{G_p} = R_s + R_p, \quad \alpha_0 = \frac{nkT}{q} + \frac{I_s}{G_p}$$

Using these coefficients, the extracted parameters are:

$$n = \frac{q(\alpha_G \alpha_0 - \alpha_G \alpha_I)}{kT(\alpha_{IG} + \alpha_I^2)}, \quad I_s = \frac{\alpha_0 - \frac{\alpha_G \alpha_0 - \alpha_G \alpha_I}{(\alpha_{IG} + \alpha_I^2)}}{\alpha_I + \frac{\alpha_{IG}}{\alpha_I}}, \quad R_s = \alpha_{VG}$$

Eq. (40) is then fitted to experimental data, where the initial values are calculated using the experimental $I - V$ characteristics. Subsequently, the coefficients in Eq. (40) are iteratively adjusted to achieve a close match between the analytical expression and the experimental values of the dynamic conductance. With the values of these coefficients, the physical parameters can be extracted via simple calculations.

Integral Method: The integral method was first developed by Ortiz-Conde et al. [84]. The integral of the current is calculated from Eq. (39):

$$\int_0^V I dx = P(V) - P(0) \quad (41)$$

where:

$$\begin{aligned} P(V) = & a_4 \left\{ \frac{a_3}{2} W^2 \left[a_1 \exp\left(\frac{V+a_2}{a_3}\right) \right] + \frac{a_6}{2a_4} V^2 + \frac{a_5}{a_4} \right. \\ & \left. + a_3 W \left[a_1 \exp\left(\frac{V+a_2}{a_3}\right) \right] \right\} \end{aligned}$$

Rearranging Eq. (39), and for $V = 0$, $I = 0$, Eq. (39) gives:

$$\begin{aligned} W \left[a_1 \exp\left(\frac{V+a_2}{a_3}\right) \right] &= \frac{I - a_6 V - a_5}{a_4}, \quad \text{and} \\ W \left[a_1 \exp\left(\frac{V+a_2}{a_3}\right) \right] &= \frac{-a_5}{a_4} \end{aligned} \quad (42)$$

By substituting Eqs. (42) into Eq. (41), Eq. (41) becomes:

$$\int_0^V I dx = c_{l1} I + c_{V1} V + c_{lV} IV + c_{l2} I^2 + c_{V2} V^2 \quad (43)$$

where:

$$\begin{aligned} c_{l1} &= a_3 \left(1 - \frac{a_5}{a_4}\right), \quad c_{V1} = \frac{a_3 a_5 a_6}{a_4} - a_3 a_6 + a_5, \\ c_{lV} &= -\frac{a_3 a_6}{a_4}, \quad c_{l2} = \frac{a_3}{2a_4}, \quad c_{V2} = \frac{a_6}{2} \left(1 + \frac{a_3 a_6}{a_4}\right). \end{aligned}$$

To obtain the values of the coefficients, the integration of Eq. (43) is calculated from the experimental $I - V$ characteristics. Next, a two-dimensional fitting process is conducted to determine the coefficients of Eq. (43) by fitting the analytical expressions to the calculated value of the integration. Finally, the physical parameters are derived from these coefficients as follows:

$$R_s = -\frac{c_{lV}}{2c_{V2}}, \quad R_p = \frac{1}{2c_{V2}}, \quad I_s = -c_{V1} - 2c_{l1}c_{V2} + c_{V1}c_{lV},$$

$$n = \frac{q}{nkT} \left(c_{l1} - \frac{c_{V1}c_{lV}}{2c_{V2}} \right)$$

The SBH can be calculated from Eq. (6) with the known value of I_s .

FindFit direct fitting: In this approach, the powerful “FindFit” function of the Mathematica software package is employed to accurately determine the Schottky parameters. The “FindFit” function is commonly used in statistics for fitting nonlinear models. The numerical values of the parameters are calculated such that a good match between the model equation and the experimental data is ensured. When dealing with linear cases, FindFit finds the global best fit. However, in nonlinear cases, it usually finds the local best fit. Many cases have proven its applicability [85,86]. The model is described by Eq. (37), and then, the physical parameters are determined by fitting the analytical expression to the experimental data. The introduction of this purely numerical, software-based method serves to compare with the former. Given the innovative nature of the first two methods, it's necessary to introduce a reference for

Table 2

Extracted parameters of different diodes using different approaches. (a) Ir-SiC Schottky diode. (b) Au-GaAs Schottky diode. (c) Organic Schottky diode. Reproduced under terms of CC-BY license [82]. Copyright 2022, Aazou et al. [82] Published by MDPI.

Materials	Parameters	Conductance	Integral	FindFit
Ir-SiC	I_s (A)	1.9×10^{-20}	1.9×10^{-20}	1.9×10^{-20}
	n	1.02	1.02	1.02
	R_s (Ω)	3.48	3.48	3.48
Au-GaAs	R_p (Ω)	3.10×10^9	3.11×10^9	3.11×10^9
	I_s (A)	4.1×10^{-17}	4.1×10^{-17}	4.1×10^{-17}
	n	1.05	1.05	1.05
Organic	R_s (Ω)	718	718	719
	R_p (Ω)	2.2×10^{10}	2.2×10^{10}	2.2×10^{10}
	I_s (A)	3.6×10^{-8}	8×10^{-8}	8 E-8
	n	5.08	5.05	5.05
	R_s (Ω)	91	91	91
	R_p (Ω)	1.632×10^4	1.632×10^4	1.632×10^4

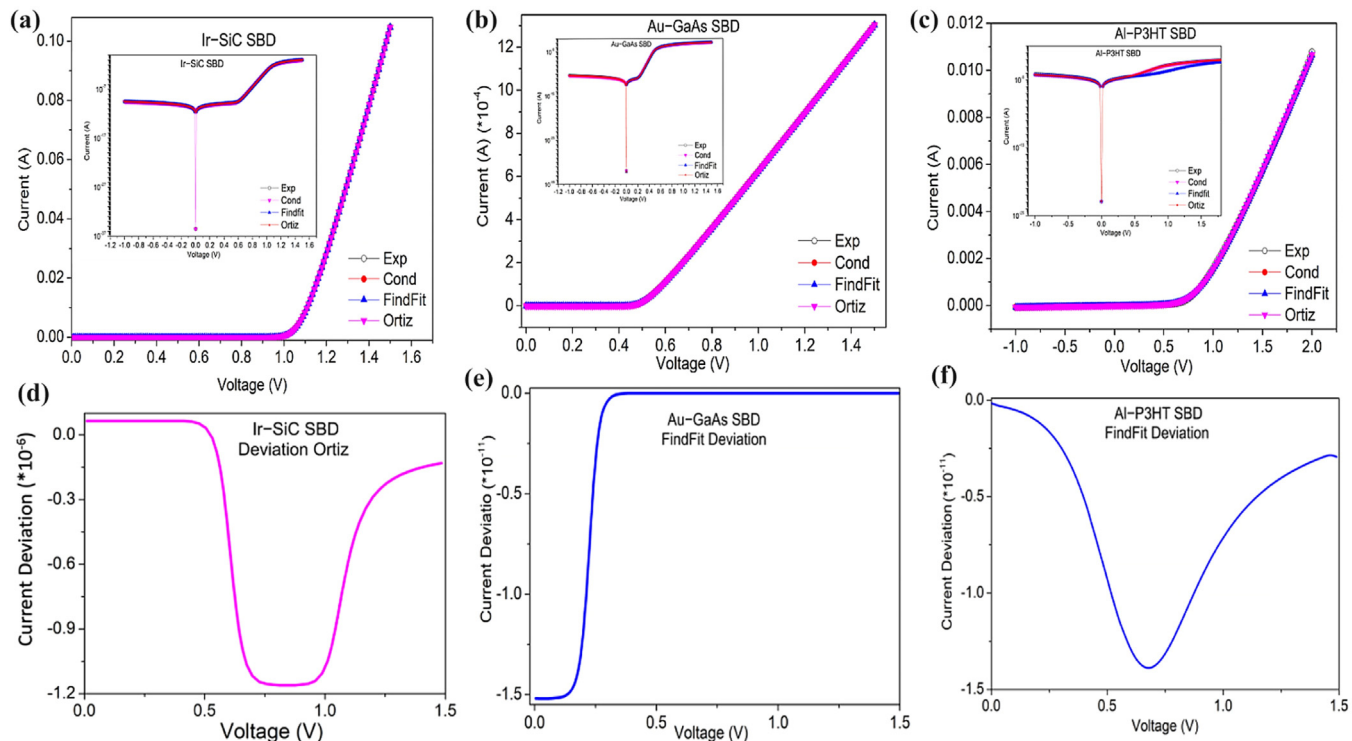


Fig. 4. Experimental data and analytic data were obtained via all 3 methods. (a) Ir-SiC Schottky diode [82]. (b) Au-GaAs Schottky diode [82]. (c) Organic Schottky diode [82]. (d) FindFit deviation of (a) [82]. (e) Ortiz method deviation of (b) [82]. (f) FindFit deviation of (c). Reproduced under terms of CC-BY license [82]. Copyright 2022, Safae Aazou et al. Published by MDPI.

assessing their scientific validity. In fact, the Findfit method is a quick parameter extraction approach. When extracting numerous sets of experiment data, this allows researchers for a relatively fast extraction procedure which can buy a lot of time. However, it may fail to extract the accurate value of the parameters in some cases. Perhaps in the future, this kind of method will be integrated into artificial intelligence (AI), and extracting the parameters may no longer need the hands of humans.

The parameters extracted using all three methods are shown in **Table 2** for comparison. The analytical characteristics generated from the extracted parameters are fitted to the experimental $I - V$ characteristics of diodes. The experimental data as well as the fittings for three different Schottky barrier diodes (SBDs) are shown in **Fig. 4(a–c)**. As shown in **Fig. 4(a, b)**, all three methods demonstrate good accuracy. This implies that for large datasets, methods such as Findfit can swiftly extract parameters. However, if discrepancies with experimental data arise, as depicted in **Fig. 4(c)**, adjustments and additional extraction steps may be necessary. All three

methods' lowest deviations are shown in **Fig. 4(d–f)**. Only the deviation shown in **Fig. 4(d)** is not acceptable. This study demonstrated that the FindFit technique yields the most accurate results for Au-GaAs Schottky diodes. However, in terms of Ir-SiC Schottky diodes, the integral technique achieves the lowest deviation. In the case of organic diodes, the first method exhibits the highest deviation, while the FindFit method achieves the lowest deviation. This result is probably obtained because the conductance method does not rely on initial values, while the integral technique requires the use of these values.

The work of Aazou et al. [82] appears to have comprehensively and accurately extracted the physical parameters of Schottky diodes. However, they seem to have overlooked the influence of both the temperature dependence and voltage dependence of the parameters introduced by inhomogeneities or other effects during model analysis [87–90]. The voltage dependence implies that the physical parameters are not merely constants but functions of the voltage. In such cases, the $I - V$ characteristic curve typically needs

to be segmented and the physical parameters extracted accordingly.

3.2. Back-to-back structured Schottky diode

The extraction approaches discussed above are for single-sided Schottky diodes. However, in practical assessment, to obtain pure single Schottky behavior, the contact between the cathode and the surface of the semiconductor side needs to be ohmic. But in practice, an additional metal contact exists while performing electrical measurements no matter whether additional electrodes were fabricated or not. What's more, ohmic contact is often hard to achieve in some cases. Thus researchers introduce the back-to-back model to describe the actual behavior of the unexpected single diode. The model describes two Schottky diodes that were placed asymmetrically with one SBH much greater than the other, in which the smaller one represents the unachieved ohmic contact. This model was then used to describe the MSM diodes as well.

3.2.1. Nouchi's method [43]

Nouchi [43] proposed that if the barrier height difference $\Delta\Phi_B$ between two MS interfaces is sufficiently large, then the lower barrier can be ignored, and the material can be treated as an MS diode. Innovatively, he developed another approach for MSM diodes when $\Delta\Phi_B$ is small, which provides an extremely simple way to extract the IF. The equivalent circuit model and band diagrams are shown in Fig. 5(a, b). The analytical $I-V$ characteristics are given by Eq. (17). The first-order derivative of Eq. (17) is given by:

$$J(V_D)' = \frac{q}{nkT} \frac{J_{st1}J_{st2}(J_{st1} + J_{st2})}{\left\{J_{st1}\exp\left[\frac{-qV_D}{2nkT}\right] + J_{st2}\exp\left[\frac{qV_D}{2nkT}\right]\right\}^2} \quad (44)$$

Nouchi [43] found that the MSM diode can be treated as a single MS diode in the same region (see Fig. 5(c, d)). Furthermore, he found an interesting relationship between the voltage drop V_{MSM} and n_2 . By replacing the current density in Eq. (14) with Eq. (16), the new equation can be approximated as follows ($V_{D1}, V_{D2} \gg nkT/q$; $V_{D1} \ll V_{D2} \approx V_{MSM}$):

$$V_{MSM} \approx n(\Phi_{B2} - \Phi_{B1}) = n_2 \Delta\Phi_B \quad (45)$$

Eq. (45) seems to be the first of its kind, in which n_2 is innovatively extracted in a very simple way. To make the equation more general, n_2 can be replaced by the n_{high} of the diode with the higher barrier. Then, Eq. (45) becomes:

$$V_{MSM} \approx n(\Phi_{B2} - \Phi_{B1}) = n_{high} \Delta\Phi_B \quad (46)$$

Nouchi [43] proposed that the parameters of MSM diodes can be extracted from an $I-V$ measurement via the following steps: (1) Extract the R_s of the MSM diode. The fitting range should be below the voltage V_H at the first local maximum in the $I-V$ curve. (2) Correct the voltage V to V_{MSM} by subtracting the voltage drop across R_s . (3) Extract the Φ_B and n_{high} values by linearly fitting the corrected $\ln(I) - V_{MSM}$ curve [43]. The fitting range should be below V_H . According to Nouchi [43], first extracting the parameters of one Schottky contact and then extrapolating them to the parameters of the other Schottky contact is relatively easy [43]. However, this method becomes ineffective when the two barrier heights are so close that distinguishing the $I-V$ curves in the same regions is difficult [45]. Additionally, this model does not account for the potential variation in the IF between the two Schottky barriers [91]. Additionally, it relies on the first and second derivatives of the device $I-V$ characteristics, which restricts its applicability [92].

3.2.2. Wangyang's method—SrR (Schottky-related resistance) function [45]

Based on the analysis of many $I-V$ curves generated from TE models (used as a database), Wangyang et al. [45] proposed an improved model for MSM diodes in practice. They innovatively proposed another way to extract the SBH when the saturation current is not reached. From Eqs. (4) and (15), the voltage drop across the MSM diode is defined by:

$$V = |V_{D1}| + |V_{D2}| + IR_s = \frac{n_1 kT}{q} \ln\left(\frac{I}{I_{st1}} + 1\right) - \frac{n_2 kT}{q} \ln\left(-\frac{I}{I_{st2}} + 1\right) + IR_s \quad (47)$$

Setting the second-order derivative of Eq. (47) equal to 0 yields:

$$I_p(V_p) = \frac{I_{st2} - \sqrt{\frac{n_2}{n_1}} I_{st1}}{1 + \sqrt{\frac{n_2}{n_1}}} \quad (48)$$

Eq. (48) implies that when slope of $I-V$ curve reaches its peak, if I_{st1} is much smaller than I_{st2} and the IFs are sufficiently close, then one can deduce $I_{st2} = 2I_p$ from Eq. (48). With the value of the saturation current, the SBH can be easily obtained.

Wangyang et al. [45] found that there exists a delicate balance between the mutual influences of these factors. The key to parameter extraction lies in minimizing the interdependence among the parameters and extracting them within a distinguishable range.

Taking the derivative of V with respect to I gives: [45]

$$\frac{dV}{dI} = SrR(I) + R_s \quad SrR(I) = \frac{n_1 kT}{q(I_{st1} + I)} + \frac{n_2 kT}{q(I_{st2} - I)} \quad (49)$$

where $SrR(I)$ is the Schottky-related resistance function (SrR), which describes the resistance caused by the two Schottky junctions in relation to the external resistance.

As shown in Fig. 5(e), when SrR is close to infinity, the current is close to saturation, and the corresponding n becomes distinguishable. The remaining parameters in the equation—IF(n_1, n_2) and R_s —can be obtained by constructing a system of simultaneous equations using three points on the $I-V$ curve. To avoid the introduction of significant errors, determining the characteristic interval and excluding the regions where the equations do not converge are crucial.

The currents I_f, I_m , and I_n in the three segments have corresponding voltages V_f, V_m , and V_n . The system of simultaneous equations is expressed as [45]:

$$V_f = \frac{n_1 kT}{q} \ln\left(\frac{I_f}{I_{st1}} + 1\right) - \frac{n_2 kT}{q} \ln\left(-\frac{I_f}{I_{st2}} + 1\right) + I_f R_s \quad (50a)$$

$$V_m = \frac{n_1 kT}{q} \ln\left(\frac{I_m}{I_{st1}} + 1\right) - \frac{n_2 kT}{q} \ln\left(-\frac{I_m}{I_{st2}} + 1\right) + I_m R_s \quad (50b)$$

$$V_n = \frac{n_1 kT}{q} \ln\left(\frac{I_n}{I_{st1}} + 1\right) - \frac{n_2 kT}{q} \ln\left(-\frac{I_n}{I_{st2}} + 1\right) + I_n R_s \quad (50c)$$

where I_f, V_f, I_m, V_m, I_n , and V_n are the data from each interval. After Eq. (50) ($f \times m \times n$ equations in total) are solved, a result group is obtained. The spectrum shows the Gaussian distribution of the possible results. However, if one or several influencing factors greatly contribute or if the data are incomplete, then deviations may occur. To fix this, Wangyang et al. [45] set n_2 as unity when solving the equations if the extracted value did not make sense.

The validity of this approach has been verified through applications. Fig. 5(f) shows the use of Wangyang et al.'s [45] method to fit an incomplete $I-V$ curve where the current did not reach saturation. To extract the SBH2, they plotted the slope of the $I-V$ curve and selected the maximum point as the I_p . The saturation current is then obtained from $I_{st2} = 2I_p$, and the SBH is consequently extracted. Fig. 5(g, h) reveals an acceptable n_1 and an unacceptable n_2 , with $n_2 = -9$. Therefore, n_2 is set to unity to solve

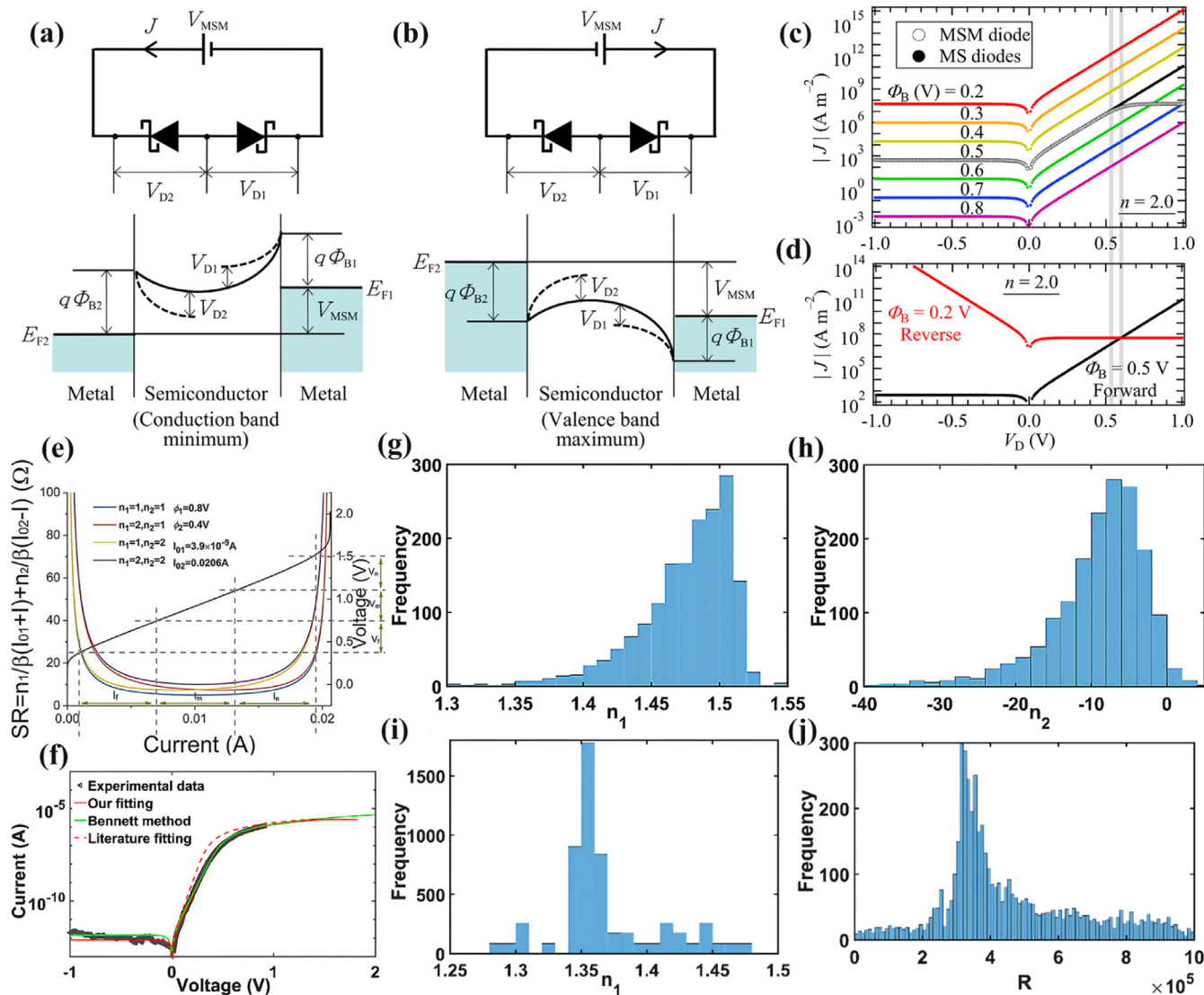


Fig. 5. (a, b) Equivalent circuits and diagrams of the conduction/valence band. (a) Reverse bias. (b) Forward bias. (c, d) Relationships between MS and MSM $I - V$ curves. (c) MS and MSM diodes with different Φ_B . (d) J of two different isolated diodes with $\Phi_B = 0.2$ V, 0.5 V, respectively [43]. (e) SrR plot with current and voltage intervals. Reproduced with permission [45]. Copyright 2014, Springer. (f–j) Wangyang et al.'s [45] extraction procedure applied to data from a published paper. (f) Final fitting compared to others. (g) Extracted n_1 before setting n_2 as unity [45]. (h) Unreliable extraction of n_2 [45]. (i) Extracted n_1 after setting n_2 as unity [45]. (j) Reliable resistance extracted. Reproduced with permission [45]. Copyright 2020, John Wiley and Sons.

the equations (the results are shown in Fig. 5(i, j)). Then, the parameters are used to compare the calculated results with the original data. Deviations can be eliminated by slightly adjusting the extracted parameters accordingly (by finding patterns in the reported database). The results agree well with the experimental data, which indicates that the approach is feasible and effective. This approach can be applied not only to MSM diodes but also to MS diodes [93]. The approach was then modified and applied to solar cells by Wangyang et al. [94]. The idea of finding the interval where the parameters are distinguishable to minimize the error and vagueness is innovative. Then, the parameter distribution spectrum is used to characterize the actual electrical behavior of the diode [95]. This idea provides new insight into the tricky extraction of Schottky parameters, making the extraction procedure more reliable and accurate.

4. Applications

The methods mentioned above can be used to accurately extract Schottky parameters to a certain extent, and these parame-

ters are very useful for analyzing the working mechanisms of different devices, such as PDs [11, 96–99], solar cells [7, 94, 100–102], nonvolatile resistive-switching devices [16, 103–105], and thin-film transistors [106–109]. Different parameters can be used for different analyses; for example, the SBH can be used for band analysis and device performance prediction, while the IF can be used for the analysis of barrier lowering [110], the interface quality [111], and carrier transport mechanisms [112]. In this section, we demonstrate the need for the extraction methods and application of these methods to show what these methods actually do and how these extraction procedures are useful. Our aim is to understand what researchers can discover through Schottky parameter extraction as well as identify strengths and weaknesses in their parameter extraction methods.

4.1. Photodetectors

In some studies, researchers often assume that for Schottky diodes made of different characteristic materials, comparing their electrical and optical characteristics is sufficient. However, the dif-

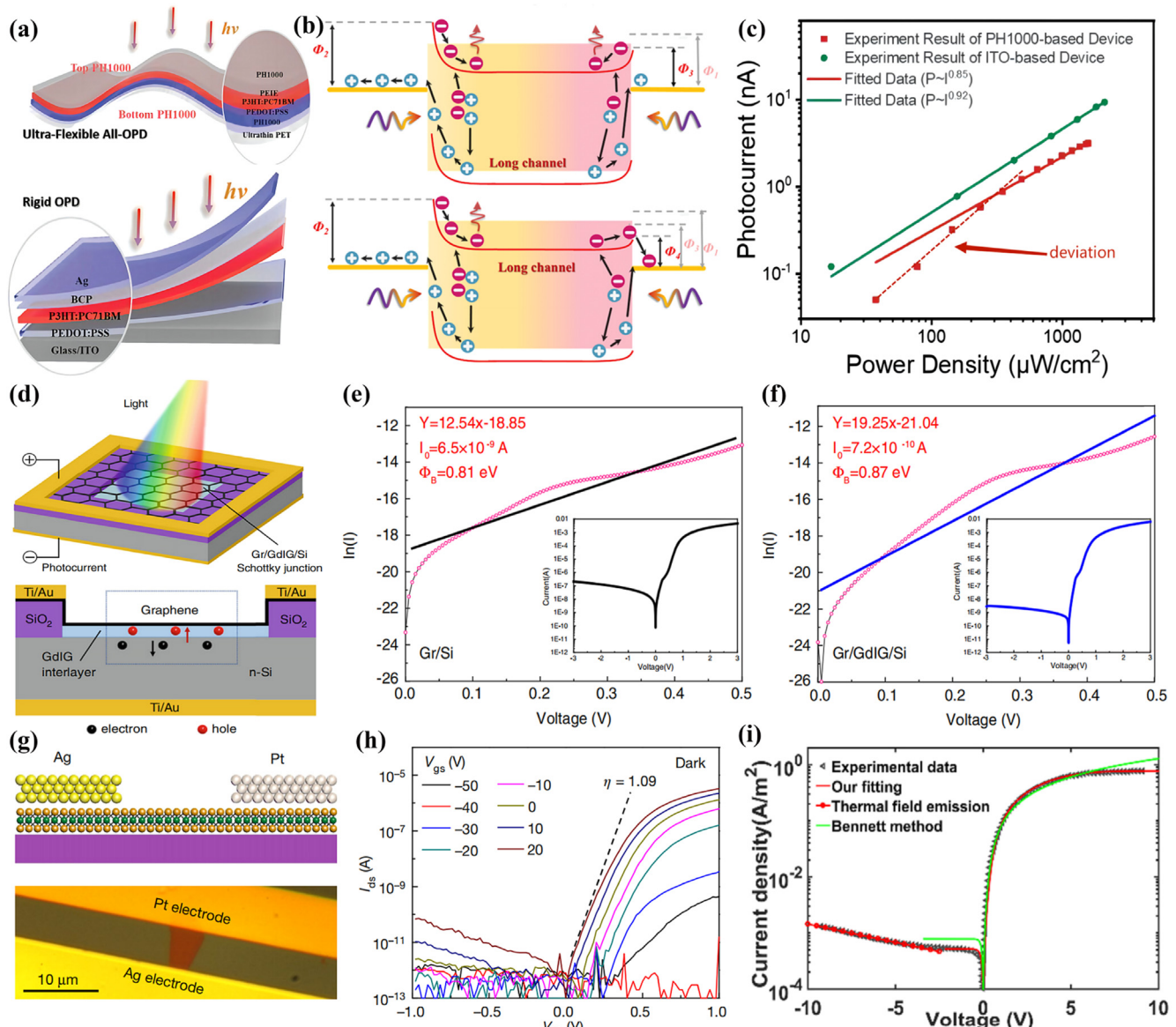


Fig. 6. (a) Optoelectronic properties of the all-organic photodetector (OPD) based on the flexible PH1000/PH1000 electrodes (upper) and rigid OPD based on ITO/Ag electrodes(lower) [97]. (b) Band diagrams of OPDs with PH1000:AgNWs and AgNWs as top electrodes [97]. (c) Photocurrent versus power density. Reproduced with permission [97]. Copyright 2022, John Wiley and Sons. (d) 3D schematic view and Cross-section of the proposed Gr/GdIG/Si photodetector [98]. (e) Semi-log $I - V$ curve (inset) and its linear fitting of Gr/Si Schottky junction to extract the parameters [98]. (f) Semi-log $I - V$ curve (inset) and its linear fitting of Gr/GdIG/Si Schottky junction. Reproduced under terms of CC-BY license [98]. Copyright 2022, Springer. (g) Schematic and optical image of asymmetric Ag-MoS₂-Pt MSM diode [99]. (h) Dark current of the device shown in (g) with IF fitted. Reproduced with permission [99]. Copyright 2018, Springer. (i) Manually picked data fitted with different methods. Reproduced with permission [45]. Copyright 2020, John Wiley and Sons.

ferences between them are relatively unanalyzed, raising questions for researchers who want to understand the reasons for these differences and then control or utilize them.

Fang's group [97] developed an ultra-flexible organic self-driven PD for biosignal detection, as shown in Fig. 6(a). The as-prepared detector reported in their paper is outstanding, but importantly, the SBH significantly determines the electrical performance, as extensively mentioned in the paper; however, they did not conduct a detailed analysis of the SBH (Fig. 6(b)) shows the band diagram of the PD and carrier behavior without the actual value of the SBH or the IF. In particular, in Fig. 6(c), the linear fits represented by the green and red lines show that both are of the same order of magnitude, but the green linear fit is excellent, while the other fit is not. This is likely due to differences in materials, which necessitates the extraction of the SBH for further analysis. The same need

for extraction was also observed in Liu et al.'s study [113]. An example of extracting the SBH can be found in Liu et al.'s work [99], where they analyzed the SBH differences between transferred and evaporated metals with various work functions, proving that the SBH of transferred MS contacts strongly depends on the metalwork function, which suggests excellent obedience to the Schottky-Mott law. Moreover, Φ_B was also extracted for Ji et al.'s graphene/silicon PD (shown in Fig. 6(d)) [98], as well as for Zhang et al.'s organic insulator device [114]. Ji et al. [98] simply applied a linear fit to the experimental data to extract Φ_B , which was then used in analyzing the band structure of the contact to study the conduction mechanism. However, notably, the linear fit does not fit the experimental data well in the range of 0.25 to 0.5 V, as shown in Fig. 6(e, f). This deviation is probably caused by the SR; hence, the range must be segmented and the fitting conducted separately [46]. A proper lin-

ear fit can be seen in Huang and Duan's study (Fig. 6(g, h)) [99], where the researchers used the IF as an interface quality indicator. They analyzed the difference in the SBH between transferred and evaporated metals with various work functions (not shown). Fig. 6(h) demonstrates they extracted an IF of $n = 1.09$, implying that the transferred metal can indeed achieve high-quality interfaces. Jiang and Luo et al. reported self-powered Schottky-based PDs [115]. They fabricated 2 %–8 % gallium source-doped CdS/Au Schottky PDs and determined that the values of n and Φ_B are 1.3–1.4 and 0.74–0.76 eV, which implies that a high-quality MS contact is obtained.

The IF is primarily a parameter describing conduction mechanisms apart from TE. An application of it can be found in Hauchecorne et al.'s study [11] on a nanowire PD, in which they fitted their electrical data using a back-to-back Schottky model, but the deviation from the ideal Schottky behavior was significant since the temperature was set at 100 °C and the device was illuminated, with $n = 157$. They assumed that the deviation from the saturation current can be attributed to a reduction in the field-induced barrier [116].

In cases where the IF significantly deviates from unity or other poor fittings (e.g., Fig. 6(e, f)), first segmenting the data and then using the proper region of the data for fitting and parameter extraction is better. Wangyang et al.'s method [45] included a Schottky-related resistance function, in which he segmented the entire region to properly solve the equations. A similar function was also used by Bhattacharya and Venimadahav to extract asymmetric Schottky parameters [117]. Wangyang et al.'s method [45] is very accurate in certain application scenarios, as shown in Fig. 6(i). The TFE model mentioned in their supplementary material can be used to describe the deviation of the current from the ideal Schottky behavior at a high bias, and the SR and IF can also be accurately extracted using the procedure shown in Fig. 5(g–j).

4.2. Solar cells

Regarding solar cell applications, Saraswat and Eric Pop's group [100] developed an outstanding flexible metal dichalcogenide solar cell (as shown in Fig. 7(a)). However, the band structure reported in Fig. 7(b) is based on a qualitative analysis rather than a quantitative analysis, which makes it lack persuasiveness. If they extracted not only n (see Fig. 7(c)) but also Φ_B , then this would help with their band analysis and electrical analysis, and the analytical work of this research would be more comprehensive. A similar application was reported by Went et al. [101], who extracted n , R_s , and R_{sh} (shown in Fig. 7(d–f)). As previously discussed, the IF can be used as an interface quality indicator, and both Ref. [100] and Ref. [101] have proven that high-quality interfaces can be obtained by extracting the IF. In Ref. [101], n and I_0 were extracted from the linear fitting shown in Fig. 7(e), and R_{sh} was extracted from the linear fitting shown in Fig. 7(f). The reported values of R_s were both negligible, indicating that good contact was obtained via the transfer of the metal. In terms of the shunt resistance, Ref. [101] suggested that through further optimization, their device can achieve less shunting based on a comparison of R_{sh} values [101].

Wang's group [102] proposed a model (shown in Fig. 7(g)) for extracting solar cell parameters. As shown in Fig. 7(h), the data are divided into four segments, A, B, C, and D, representing regions dominated by different mechanisms, namely, the shunt current, recombination current, diffusion current, and diffusion current limited by the SR [102]. The fit obtained with their model is excellent, but the fitting did not consider the SR, unfortunately leading to a lack of fit in Region D; however, this provides an opportunity for subsequent researchers. For extraction of the SR, they used a linear fitting method, as shown in Fig. 7(i), and the value of the SR can be obtained by calculating the intercept of the linear fit [102]. A sim-

ilar method was also described by Wangyang's group [94] in their study on solar cell parameter extraction (Fig. 7(k)). Their extraction method has universally improved the fitting accuracy compared to previous studies, as shown in Fig. 7(j), which demonstrates the accuracy of the extraction procedure.

4.3. Resistive-switching memories

Recently, great progress has been made in nonvolatile resistive-switching memories. The introduction of MS contacts makes the analysis of their electrical characteristics difficult, hence emphasizing the need for Schottky parameter extraction. Fig. 8(a–c) shows the nonvolatile resistive-switching atomistor developed by Akinwande's group [16], which provides prospects for the next generation of solid-state memory. Fig. 8(b) demonstrates the resistive-switching characteristics of the device, while Fig. 8(c) shows the linear fit in the high-resistance state (HRS) [16]. However, their fitting model did not consider the influence of the IF or SR. Additionally, in the low-resistance state (LRS), according to their research, the conduction of charge carriers mainly depends on the tunneling mechanism, which urgently requires confirmation analysis of the IF and tunneling model for this mechanism. A similar need is seen in Min et al.'s research [104] on ferromagnet-silicon spin-tunnel contacts (shown in Fig. 8(f, g)) where they managed to tune the SBH through the Gd thickness while ignoring the IF and SR.

Xi et al. [103] successfully extracted both the IF and SBH for analysis of the device mechanism and provided an example of extracting these parameters. They achieved ferroelectric modulation by engineering the SBH through interfacial states, namely, ON and OFF states (Fig. 8(d, e)). Through the extraction of the IF, they found that it decreases as the doping concentration decreases, as shown in Fig. 8(e), while the depletion region thickness exhibits the opposite trend. They determined that this trend is due to the different depletion region thicknesses in the ON and OFF states and thus the different SBHs, with the SBH even completely disappearing in the ON state (not shown). Therefore, their analysis is relatively comprehensive. In contrast, Huh et al. [105] (Fig. 8(h–j)) reported a memristor that mimics synaptic behavior. Fig. 8(i) demonstrates the switching ability of their device, while Fig. 8(j) shows the gate-tunable SBH behavior. Unfortunately, the exact switching mechanism was not explained in the article, and as shown in the inset in Fig. 8(j), the tunability of the SBH was not statistically verified. Hence, extraction of Schottky parameters is urgently needed in this work.

4.4. Thin-film transistors

Thin-film transistors are known for their extraordinary performance and fascinating structures. Due to the two-dimensional nature of thin films, researchers have fabricated various excellent thin-film transistors by stacking different materials in recent years. The device shown in Fig. 9(a) is an example of a stack prepared by Wei et al. [106]. They reported a pseudo-complementary metal-oxide-semiconductor (CMOS) that has a tunable barrier induced by a gapped channel. The IF was estimated to be 1.1 in their work, indicating excellent rectification performance (shown in Fig. 9(b)) [106]. However, the gap-induced barrier, which causes an ultralow reverse saturation current, was not explained, at least not statistically, raising questions for readers. Hence, extraction of the SBH is needed. A similar need can be seen in the work of Zhang et al. [107]. Ref. [107] reported a MoS₂/WTe₂ FET biosensor (as shown in Fig. 9(c, d)). When the DNA chain concentration changes, the SBH is modified through the change in the width of the depletion region. Hence, the current changes (as shown in Fig. 9(d)) [107]. Although their qualitative analysis is comprehensive and persuasive, the changes in the SBH still need to be extracted to validate

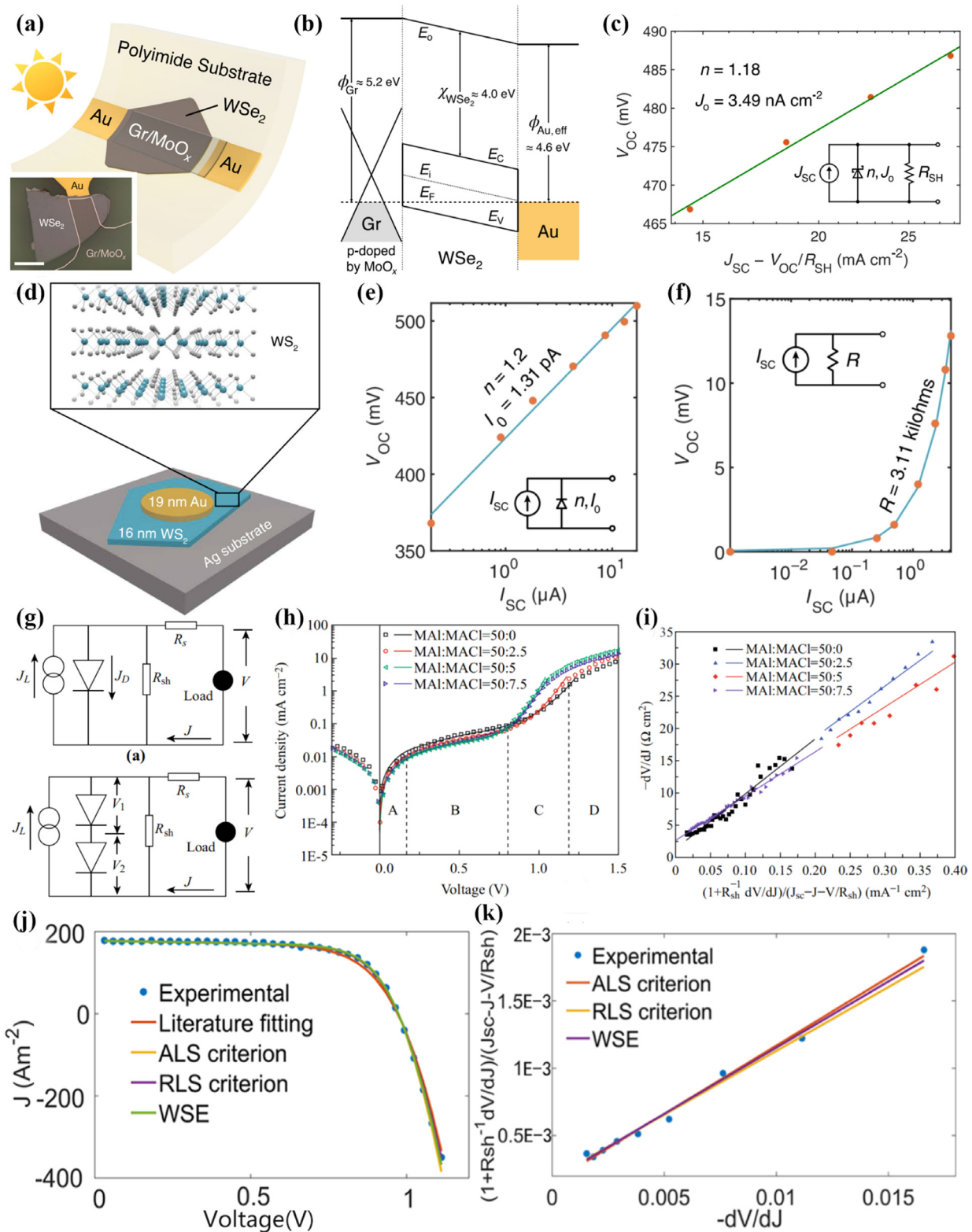


Fig. 7. (a) Schematic of metal dichalcogenide solar cell, inset shows the optical image of the device [100]. (b) Qualitative energy band diagram of the device [100]. (c) Open-circuit voltage versus diode current density, inset shows the equivalent circuit of the device. Red dots represent experimental data, green line represents linear fit. Reproduced under the term of CC-BY license [100]. Copyright 2021, Nazif et al. [100] Springer.

(d) Schematic of vertical Schottky-junction multilayer WS_2 solar cells with transferred contacts [101]. (e, f) The Open-circuit voltage of devices with transferred (e) and evaporated (f) Au contacts. Symbols, measurements; line, fit. Insets show representative circuit diagrams. Reproduced with permission [101]. Copyright 2019, American Association for the Advancement of Science.

(g) Equivalent circuit of single (upper) and double (lower) junction planer solar cells (PSCs) [102]. (h) Dark $J - V$ curves of perovskite PSCs with different concentrations of Cl ions. Fitting curve by article model [102]. Regions A, B, C, and D are shunt current, recombination current, diffusion current, and diffusion current limited by SR.

(i) Plot of $-dV/dJ$ versus $(1+R_{sh}^{-1}dV/dJ)/(J_{sc}-J-V/R_{sh})$ ($\text{mA}^{-1} \text{cm}^2$) for MAI:MACl = 50:0, 50:2.5, 50:5, and 50:7.5.

(j) Plot of J (Am^{-2}) versus Voltage (V) for Experimental data, Literature fitting, ALS criterion, RLS criterion, and WSE.

(k) Plot of swapped $-dV/dJ$ versus $-dV/dJ$ for Experimental data and fitted curves by ALS criterion, RLS criterion, and WSE.

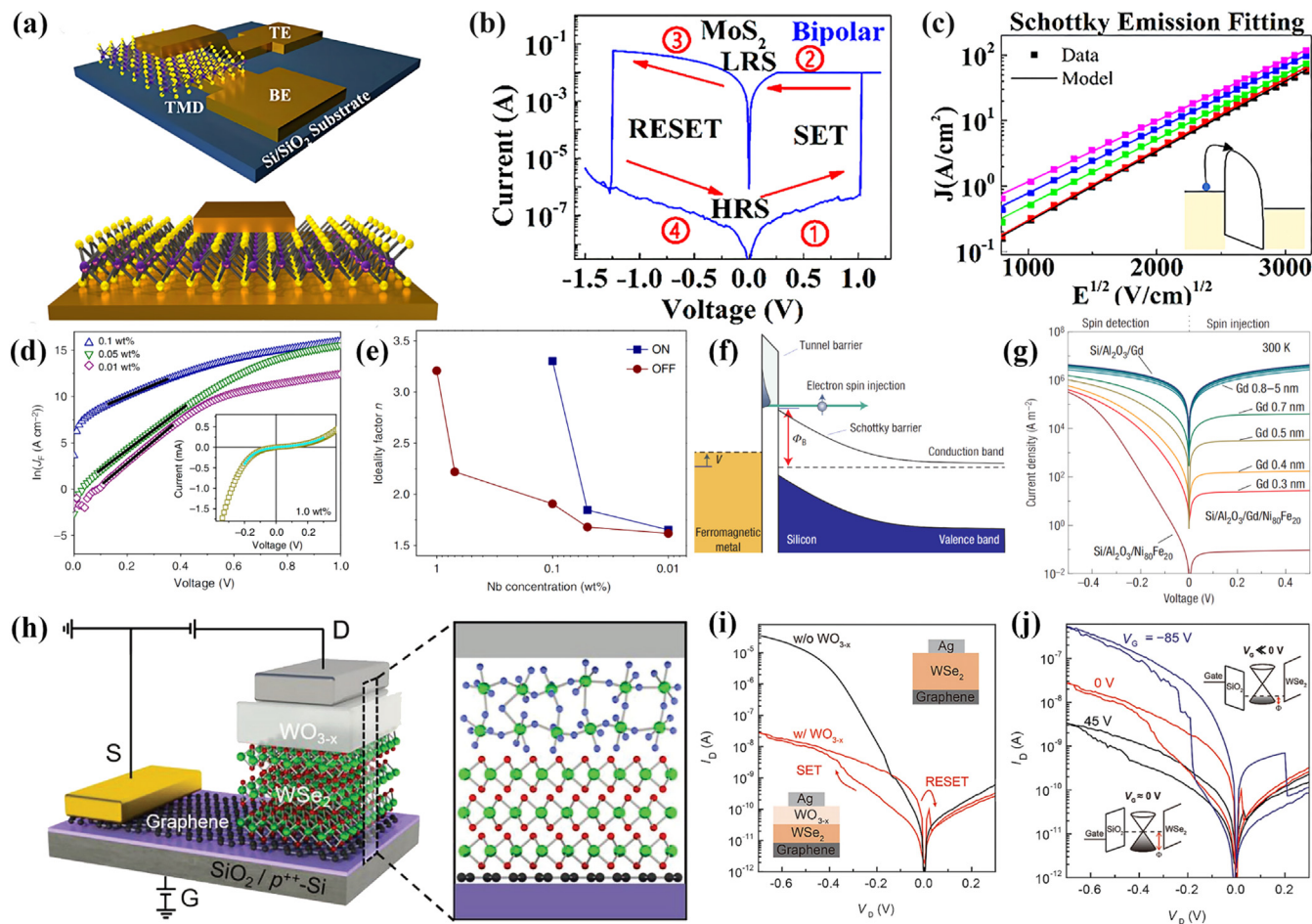


Fig. 8. Schematics and plots reprinted with permissions. (a) Schematic of Transitional-metal-dichalcogenide (TMD) metal-insulator-metal structure [16]. (b) $I - V$ curve of bipolar resistive switching behavior in the device shown in (a). Step 1: At ~ 1 V, the current abruptly increases to compliance current, indicating a transition (set) from a high resistance state (HRS) to a low resistance state (LRS). Steps 2 and 3: The device remains in LRS. When voltage decreases from 0 to -1.5 V. At -1.25 V, the current abruptly decreases, indicating a transition (reset) from LRS to HRS. Step 4: voltage decreases from -1.5 to 0 V. The device remains in HRS until the next cycle [16]. (c) Fitted data using the TE model for HRS. The X-axis is the electric field across the dielectric. The inset shows the carrier transportation of the TE model. Reprinted with permission from Ref. [16]. Copyright 2018, American Chemical Society. (d) $\ln J_f - V$ plots for the ON states. Black solid lines represent fits to Eq. (16) in terms of $V_0 \gg kT/q$. The inset shows the ON state $I - V$ curve of the junction with an Nb concentration of 1.0 wt%, the solid line is fit to the direct tunneling model [103]. (e) IF extracted from the fitting of different Nb concentrations. Reproduce under terms of CC-BY license [103]. Copyright 2018, Xi et al. [103] Springer. (f) Energy band diagram of electron spin injection [104]. (g) Absolute value of current density versus bias voltage of different contacts. The minus voltage is the forward bias (the spin-detection condition); the positive voltage is the reverse bias (the spin-injection condition). Reproduced with permission [104]. Copyright 2006, Springer. (h) Schematic representation of diagrams of the synaptic barristor consisting of a vertically integrated WO_{3-x} memristor and $\text{WSe}_2/\text{graphene}$ barristor [105]. (i) $I_D - V_D$ curves of the devices with (red line) and without a WO_{3-x} layer (black line). Insets show the schematic of the diagrams of the devices. The "SET" and "RESET" processes are indicated by the up and down arrows, respectively [105]. (j) Switching $I_D - V_D$ curves at various V_G values of -85 , 0 , and 45 V. The V_{SET} values are indicated by the dashed arrows. The inset shows band diagrams for the graphene/ WSe_2 junction when $V_G \approx 0$ V (left) and $V_G \ll 0$ V (right). Reproduced with permission [105]. Copyright 2018, John Wiley and Sons.

this analysis. After the SBH is extracted, it can be compared with the expected value (the difference between the metal work function and the semiconductor affinity energy) to determine whether there is a pinning effect, although the pinning effect is often weak at van der Waals (vdW) junctions [118]. Thus, this provides a possibility for predicting the working mechanism of the device. An example of extracting the SBH is shown in Fig. 9(e, f), where the expected value of Φ_B agrees with the extracted value [108]. Ref. [108] reported that compared to conventional organic field-effect transistors (FETs) with an ohmic contact, their device has significantly reduced static energy consumption due to the Schottky barrier, which they extracted and verified [108]. Additionally, they found that the Schottky barrier also resulted in extremely low static noise (in a dark environment), as hole injection was blocked by the barrier (Fig. 9(f)) [108]. Similarly, in Nathan and Lee's work [109], they also extracted the SBH and used it to analyze the effective SBH lowering with increasing V_{GS} (as shown in Fig. 9(g-i)), exquisitely elucidating the working mechanism and principles

of the MSM diode. However, as discussed in Section 4.1, extraction of the IF is also important for interface evaluation and mechanism explanation, which seems to not have been performed in Refs. [107–109]. The benefits of extracting the IF can be seen in the study of Myeong et al. [119] on a Dirac-source diode with a subunity IF. Additionally, Milano et al. [120] meticulously analyzed the electrical characteristics of ZnO nanowire Schottky diodes. They used four different methods to extract the Schottky parameters, among which the $I - V - T$ method and Cheung et al.'s method [40] yielded similar Ifs. At the same time, they found that the IF decreases with increasing temperature, while the SBH exhibits the opposite behavior. This temperature dependence can be attributed to inhomogeneities at the interface and can be explained by the potential fluctuation model. This study also revealed the existence of a dual Gaussian distribution of the SBH [120]. Moreover, the authors proposed that the temperature dependence of the reverse saturation current is caused by thermally activated conduction mechanisms [120]. Their analysis is rather comprehensive, and

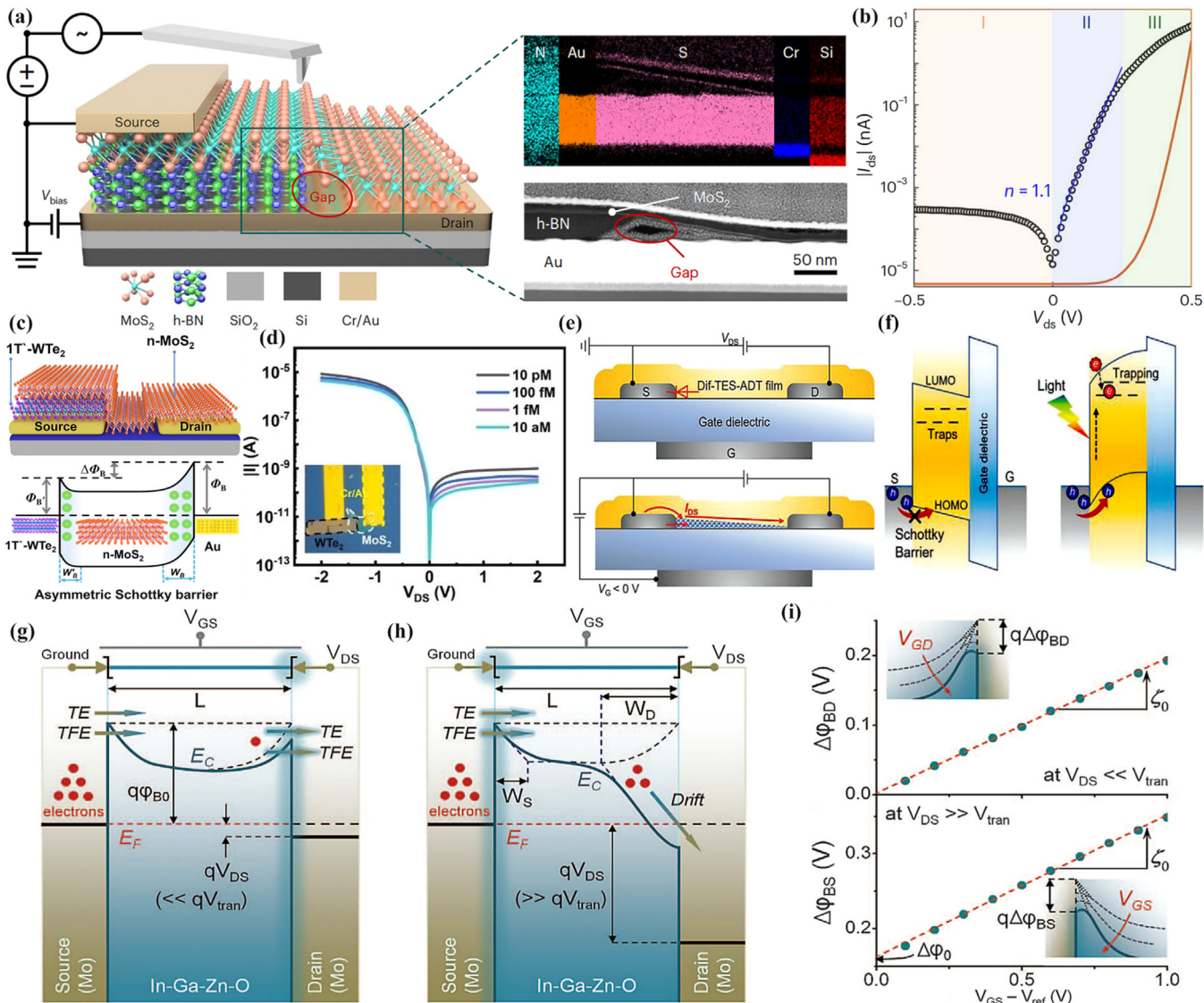


Fig. 9. (a) Schematic of homojunction inverter based on self-biased molybdenum disulfide transistor prepared by Zhang's group [106]. The zoomed-in image shows the transmission electron microscope analysis and energy-dispersive spectrometer mapping. (b) $I - V$ curve and partial fitting curve (blue line) of the homojunction with three regions: (I) reverse saturation current region. (II) Forward ideal diode region. (III) forward SR dominant region. The IF of $n = 1.1$ is extracted from the region (II). Reproduced with permission [106]. Copyright 2024, Springer. (c) Schematic diagram of the MoS₂/WTe₂ FET biosensor (upper) and the band diagram of the structure (lower) [107]. (d) Output characteristic curves of the device. The inset shows the false color SEM image. Reproduced under terms of CC-BY license [107]. Copyright 2024, MDPI. (e) Schematic of the reported organic FET under no V_G (upper) and $V_G < 0$ (lower) [108]. (f) Illustration of energy band diagrams of 2,8-difluoro-5,11-bis-(triethylsilylethynyl)anthradithiophene (Dif-TES-ADT) and perfluorobenzenothiol (PFBT)-treated Ag electrodes before (left) and after (right) light illumination. Reproduced with permission [108]. Copyright 2022, John Wiley and Sons. (g) Band diagram under $V_{DS} < V_{tran}$ [109]. (h) Band diagram under $V_{DS} > V_{tran}$ [109]. (i) Retrieved $\Delta\Phi_{BD}$ at drain contact as a function of $V_{GS} - V_{ref}$ (upper). Extracted $\Delta\Phi_{BS}$ at source contact as a function of $V_{GS} - V_{ref}$ (lower). Insets are schematic diagrams to describe the bias-dependent SB lowering at drain and source contact, respectively. Reproduced with permission [109]. Copyright 2016, American Association for the Advancement of Science.

the underlying mechanisms have been explored and explained. The same is true for the model proposed by Bartolomeo et al. [92]. Although the expected negative SBH was not extracted, the parameters of MoS₂, WSe₂, and WS₂ Schottky diodes were rather accurately obtained.

5. Outlook

Challenges and difficulties remain in the field of Schottky contact parameter extraction. Every method we have discussed can be used to carefully and accurately extract the SBH in the applicable range of the method. For example, in the field of PDs, there are already relatively sophisticated extraction methods, such as the approach of Wangyang et al. [45]. However, there are still shortcomings, particularly for low dimensions and small sizes, where

the need to introduce additional conduction mechanisms, such as TFE [121–123], FE [124,125], and tunneling effects [126] is evident. These studies were carried out to obtain a better understanding, yet few could utilize the models and extract parameters with them.

In terms of perovskite solar cells, researchers have proposed models for detailed mechanism analysis and parameter extraction, such as in Ref. [102]. Subsequent studies in this direction need to focus on the impact of different materials on the performance and parameters due to their unique interface characteristics. When necessary, new conduction mechanisms such as quantum tunneling can be introduced to analyze special materials [127,128].

When extracting the parameters of Schottky-based resistive-switching memories (RSMs), the extraction procedures must be able to accurately extract the SR of the RSM while considering the

electric field induced by interface defects [129,130]. Moreover, the extraction of the SBH and IF cannot be overlooked. Similarly, when extraction procedures are applied to FETs, the procedures also need to account for the impacts of the interface states on the SBH and IF as well as the tunneling effect, as previously discussed.

Future research in this area will need to focus on integrating these methods while maintaining their merits and even on applying them to various types of devices, such as organic materials [131,132], and hybrid materials [133]. For these devices, their differences must be considered and targeted modifications or new extraction methods proposed. Furthermore, a single extraction method may not be fully applicable to the same device under different operating conditions (such as different voltages and temperatures). In such cases, segmentation of the data must be considered, and if necessary, different methods must be used for different segments. Special problems require special treatment to build more accurate models and thus extract parameters more accurately. Additionally, based on previous experimental data and experience, researchers can also build a database and utilize AI data analysis and deep learning for parameter extraction, which may indeed be a future trend.

6. Conclusions

As discussed, several methods for extracting Schottky contact parameters have been reviewed, and their applications have been examined. These methods include both well-known, widely used methods, and relatively new methods. Every method is reviewed, with a comprehensive introduction of the theoretical analysis and an objective appraisal of the accuracy, effectiveness, feasibility, and disadvantages. Norde was the first to use a different approach to highlight the impact of high resistance and extract it, but this approach might have high inaccuracy because few data points are selected [37]. Lien et al. [38] and Bolin [39] used more data to modify Norde's method to avoid errors introduced by uncertainties. However, their methods are limited by the range of the voltage drop across the diode. Cheung et al. [40] seem to have been the first to apply the derivative of the $I - V$ characteristics to extract Schottky parameters. Two plots, which indirectly prove the consistency of the approach, are used to extract all the parameters, which is currently one of the most useful approaches for extracting Schottky parameters. Werner's method [70] innovatively considers the impact of the shunt resistance. Although this approach has some restrictions and inaccuracies in many cases, it still provides new insights into the extraction of parameters. Osvald et al. [41] and Liou et al. [42] proposed two relatively new methods called vertical and lateral optimization. By averaging the error across the entire range, they managed to extract the values of the SBH and SR, with the IF assumed to be unity (they assumed that there were no other current transport mechanisms apart from TE). Their approaches are purely numerical, which bypasses the need to plot several curves and find linear parts. Aazou et al. [82] expressed Schottky diode $I - V$ characteristics in the form of a LambertW function and simplified the function by defining new coefficients. The values of the parameters were calculated from the coefficients obtained by fitting the function to experimental data. In terms of MSM Schottky diodes, two methods were reviewed: those of Nouchi [43] and Wangyang et al. [45]. Nouchi's method [43] is fast and convenient, but it overlooks the difference between the IFs of the two contacts. Wangyang et al. [45] found that to accurately distinguish Schottky parameters, they must be extracted within a specific interval. Within this interval, a system of equations is solved, and the spectrum of results is plotted. They could identify the most likely values of the parameters and then reuse them to fit the equation to experimental data. Wangyang's method [45] is accurate and effective and can be applied to both MSM and MS diodes.

In conclusion, the Schottky parameter extraction methods proposed by previous researchers are highly practical and exhibit considerable accuracy. By using their methods, the Schottky parameters of the most common devices can be extracted. However, with the advancement of research, certain methods will no longer be applicable or may be found to contain some errors. This will necessitate subsequent researchers to stand on the shoulders of their predecessors, refine the extraction methods, and establish more universally applicable models for extracting Schottky parameters.

Declaration of competing interest

The authors declare that they have no known competing financial interests or personal relationships that could have appeared to influence the work reported in this paper.

CRediT authorship contribution statement

Peihua Wangyang: Writing – original draft, Resources, Investigation, Formal analysis, Data curation, Conceptualization. **Xiaolin Huang:** Visualization, Validation, Software, Resources, Investigation, Formal analysis, Data curation. **Xiao-Lei Shi:** Writing – review & editing, Visualization, Resources, Methodology, Formal analysis, Data curation. **Niuniu Zhang:** Formal analysis, Data curation. **Yu Ye:** Resources, Formal analysis, Data curation. **Shuangzhi Zhao:** Formal analysis, Data curation. **Jiamin Zhang:** Formal analysis. **Yingbo Liu:** Formal analysis. **Fabi Zhang:** Data curation. **Xingpeng Liu:** Data curation. **Haiou Li:** Formal analysis. **Tangyou Sun:** Supervision, Project administration, Investigation, Funding acquisition, Formal analysis, Conceptualization. **Ying Peng:** Writing – original draft, Visualization, Validation, Supervision, Project administration, Investigation, Funding acquisition, Formal analysis, Data curation, Conceptualization. **Zhi-Gang Chen:** Writing – review & editing, Validation, Project administration, Investigation, Formal analysis, Conceptualization.

Acknowledgments

This work was financially supported by Guangxi Science and Technology Plan Project (Nos. AD21220150, 2023GXNSFBA026216, AD21220056, and 2023JJG170001), the National Natural Science Foundation of China (Nos. 51802032, 52262022, 52061009, 62174041, and 62361022), the Yunnan Province Major Science and Technology Projects (No. 202102AB080008-2). Zhi-Gang Chen thanks the financial support from the Australian Research Council and QUT Capacity Building Professor Program. This work was enabled by the use of the Central Analytical Research Facility hosted by the Institute for Future Environments at QUT.

References

- [1] F. Schwierz, J.J. Liou, Microelectron. Reliab. 41 (2001) 145–168.
- [2] T.W. Crowe, R.J. Mattauch, H. Roser, W.L. Bishop, W.C. Peatman, X. Liu, Proc. IEEE 80 (1992) 1827–1841.
- [3] S.J. Yang, K.-T. Park, J. Im, S. Hong, Y. Lee, B.-W. Min, K. Kim, S. Im, Nat. Commun. 11 (2020) 1574.
- [4] A.M. Bagher, Am. J. Opt. Photo. 3 (2015) 94–113.
- [5] T. Feng, D. Xie, Y. Lin, Y. Zang, T. Ren, R. Song, H. Zhao, H. Tian, X. Li, H. Zhu, Appl. Phys. Lett. 99 (2011) 233505.
- [6] G. Li, Z. Su, L. Canil, D. Hughes, M.H. Aldamasy, J. Dagar, S. Trofimov, L. Wang, W. Zuo, J.J. Jerónimo-Rendon, Science 379 (2023) 399–403.
- [7] F. Zhang, T. Song, B. Sun, Nanotechnology 23 (2012) 194006.
- [8] J. Min, S. Demchyshyn, J.R. Sempionatto, Y. Song, B. Hailegnaw, C. Xu, Y. Yang, S. Solomon, C. Putz, L.E. Lehner, Nat. Electron. 6 (2023) 630–641.
- [9] B. Ezhilmaran, A. Patra, S. Benny, M.R. Sreelakshmi, V.V. Akshay, S.V. Bhat, C.S. Rout, J. Mater. Chem. C 9 (2021) 6122–6150.
- [10] Q. Xu, X. Wang, H. Zhang, W. Shao, J. Nie, Y. Guo, J. Wang, X. Ouyang, ACS Appl. Electron. Mater. 2 (2020) 879–884.
- [11] P. Haucercorne, F. Gity, M. Martin, H. Okuno, S. Bhattacharjee, J. Moeyaert, D. Rouchon, B. Hyot, P.K. Hurley, T. Baron, A.C.S. Appl. Nano Mater. 4 (2021) 7820–7831.

- [12] L. Ai, Y. Pei, Z. Song, X. Yong, H. Song, G. Liu, M. Nie, G.I. Waterhouse, X. Yan, S. Lu, *Adv. Sci.* 10 (2023) 2207688.
- [13] L. Yuan, S. Liu, W. Chen, F. Fan, G. Liu, *Adv. Electron. Mater.* 7 (2021) 2100432.
- [14] F. Ghafoor, M. Ismail, H. Kim, M. Ali, S. Rehman, B. Ghafoor, M.A. Khan, H. Patil, S. Kim, M.F. Khan, *Nano Energy* 122 (2024) 109272.
- [15] T. Sun, F. Yu, X. Tang, H. Li, F. Zhang, Z. Xu, Q. Liao, Z. Yu, X. Liu, P. Wangyang, *J. Materiomics* 10 (2023) 440–447.
- [16] R. Ge, X. Wu, M. Kim, J. Shi, S. Sonde, L. Tao, Y. Zhang, J.C. Lee, D. Akinwande, *Nano Lett.* 18 (2018) 434–441.
- [17] X. Wu, Y. Gu, R. Ge, M.I. Serna, Y. Huang, J.C. Lee, D. Akinwande, *NPJ 2D Mater. Appl.* 6 (2022) 31.
- [18] B. Hu, X.-L. Shi, J. Zou, Z.-G. Chen, *Chem. Eng. J.* 437 (2022) 135268.
- [19] G. Liu, L. Wang, C. Sun, Z. Chen, X. Yan, L. Cheng, H.-M. Cheng, G.Q. Lu, *Chem. Commun.* (2009) 1383–1385.
- [20] W.-D. Liu, Y. Yu, M. Dargusch, Q. Liu, Z.-G. Chen, *Renew. Sust. Energ. Rev.* 141 (2021) 110800.
- [21] H. Xue, Q. He, G. Jian, S. Long, T. Pang, M. Liu, *Nanoscale Res. Lett.* 13 (2018) 1–13.
- [22] A. Itoh, H. Matsunami, *Phys. Stat. Sol. A* 162 (1997) 389–408.
- [23] W. Walukiewicz, *J. Vac. Sci. Technol. B* 5 (1987) 1062–1067.
- [24] L. Brillson, H. Mosbacher, M. Hetzer, Y. Strzhemechny, G. Jessen, D. Look, G. Cantwell, J. Zhang, J. Song, *Appl. Phys. Lett.* 90 (2007) 102–116.
- [25] X. Pan, Y. Li, B. Cheng, S.-J. Liang, F. Miao, *Sci. China Phys. Mech. Astron.* 66 (2023) 117504.
- [26] T. Xu, Y. Wang, Z. Xiong, Y. Wang, Y. Zhou, X. Li, *Nanomicro Lett.* 15 (2022) 6.
- [27] L. Yang, Y. Jin, Z. Fang, J. Zhang, Z. Nan, L. Zheng, H. Zhuang, Q. Zeng, K. Liu, B. Deng, H. Feng, Y. Luo, C. Tian, C. Cui, L. Xie, X. Xu, Z. Wei, *Nanomicro Lett.* 15 (2023) 111.
- [28] H.M. Manohara, E.W. Wong, E. Schlecht, B.D. Hunt, P.H. Siegel, in: Proceedings to the Joint 30th International Conference on Infrared and Millimeter Waves/13th International Conference on Terahertz Electronics, Williamsburg, VA, 2005, pp. 285–286.
- [29] T.W. Crowe, R.J. Mattauch, H.P. Roser, W.L. Bishop, W.C.B. Peatman, X.L. Liu, *Proc. IEEE* 80 (1992) 1827–1841.
- [30] M.K. Das, C. Capell, D.E. Grider, R. Raju, M. Schutten, J. Nasadoski, S. Leslie, J. Ostop, A. Hefner, in: Proceedings to the IEEE Energy Conversion Congress and Exposition (ECCE), Phoenix, AZ, 2011, pp. 2689–2692.
- [31] S. Wang, X. Pan, L. Lyu, C.-Y. Wang, P. Wang, C. Pan, Y. Yang, C. Wang, J. Shi, B. Cheng, *ACS Nano* 16 (2022) 4528–4535.
- [32] A.K. Geim, I.V. Grigorieva, *Nature* 499 (2013) 419–425.
- [33] H. Lim, S.I. Yoon, G. Kim, A.-R. Jang, H.S. Shin, *Chem. Mater.* 26 (2014) 4891–4903.
- [34] E.H. Rhoderick, R.H. Williams, *Metal-semiconductor Contacts*, 2nd ed., Clarendon Press, New York, 1988.
- [35] V. Aubry, F. Meyer, *J. Appl. Phys.* 76 (1994) 7973–7984.
- [36] O.Y. Olikh, *J. Appl. Phys.* 118 (2015) 024502.
- [37] H. Norde, *J. Appl. Phys.* 50 (1979) 5052–5053.
- [38] C.-D. Lien, F. So, M.-A. Nicolet, *IEEE Trans. Electron Devices* 31 (1984) 1502–1503.
- [39] K. Bohlin, *J. Appl. Phys.* 60 (1986) 1223–1224.
- [40] S. Cheung, N. Cheung, *Appl. Phys. Lett.* 49 (1986) 85–87.
- [41] J. Osvald, E. Dobrocka, *Semicond. Sci. Technol.* 11 (1996) 1198.
- [42] A. Ortiz-Conde, Y. Ma, J. Thomson, E. Santos, J. Liou, F.G. Sánchez, M. Lei, J. Finol, P. Layman, *Solid-State Electron.* 43 (1999) 845–848.
- [43] R. Nouchi, *J. Appl. Phys.* 116 (2014) 184505.
- [44] R. Bennett, *IEEE Trans. Electron Devices* 34 (1987) 935–937.
- [45] Z. Wang, W. Zang, Y. Shi, X. Zhu, G. Rao, P. Wangyang, J. Chu, C. Gong, X. Gao, H. Sun, *Phys. Stat. Sol. A* 217 (2020) 1901018.
- [46] D.K. Schroder, *Semiconductor Material and Device Characterization*, 3rd ed., John Wiley & Sons, Hoboken, 2005.
- [47] J.H. Werner, H.H. Gütterl, *J. Appl. Phys.* 69 (1991) 1522–1533.
- [48] M. Missous, E.H. Rhoderick, *J. Appl. Phys.* 69 (1991) 7142–7145.
- [49] G. Liang, T. Cui, K. Varahramyan, *Solid-State Electron.* 47 (2003) 691–694.
- [50] W. Spicer, I. Lindau, P. Skeath, C. Su, P. Chye, *Phys. Rev. Lett.* 44 (1980) 420.
- [51] H. Card, E. Rhoderick, *J. Phys. D: Appl. Phys.* 4 (1971) 1589.
- [52] C. Henry, R. Logan, F. Merritt, *J. Appl. Phys.* 49 (1978) 3530–3542.
- [53] X.-L. Tang, H.-W. Zhang, H. Su, Z.-Y. Zhong, *Physica. E: Low Dimens. Syst. Nanostruct.* 31 (2006) 103–106.
- [54] A.J. Chiquito, C.A. Amorim, O.M. Berengue, L.S. Araujo, E.P. Bernardo, E.R. Leite, *J. Phys.: Condens. Matter* 24 (2012) 225303.
- [55] H.J. Werner, P.J. Knowles, *J. Chem. Phys.* 89 (1988) 5803–5814.
- [56] P. Blom, R. Wolf, J. Cillesken, M. Krijn, *Phys. Rev. Lett.* 73 (1994) 2107.
- [57] A. Di Bartolomeo, G. Luongo, F. Giubileo, N. Funicello, G. Niu, T. Schroeder, M. Lisker, G. Lupina, *2D Mater.* 4 (2017) 025075.
- [58] D. Korucu, A. Turut, H. Efeoglu, *Phys. B: Condens. Matter.* 414 (2013) 35–41.
- [59] K. Sato, Y. Yasumura, *J. Appl. Phys.* 58 (1985) 3655–3657.
- [60] F. Padovani, G. Sumner, *J. Appl. Phys.* 36 (1965) 3744–3747.
- [61] R. Hackam, P. Harrop, *IEEE Trans. Electron Devices* 19 (1972) 1231–1238.
- [62] A. Büyükbaba Uluşan, A. Tataroğlu, Y. Azizian-Kalandaragh, Ş. Altindal, *J. Mater. Sci.: Mater. Electron.* 29 (2018) 159–170.
- [63] A. Sinha, J. Poate, *Appl. Phys. Lett.* 23 (1973) 666–668.
- [64] Ş. Aydoğan, Ü. İncekara, A.R. Deniz, A. Türüt, *Microelectron. Eng.* 87 (2010) 2525–2530.
- [65] K. Zeghdar, L. Dehimi, A. Saadoune, N. Sengouga, *J. Semicond.* 36 (2015) 124002.
- [66] A. Turut, M. Saglam, H. Efeoglu, N. Yalcin, M. Yildirim, B. Abay, *Physica B: Condens. Matter* 205 (1995) 41–50.
- [67] H. Patel, K. Patel, A. Patel, H. Jagani, K.D. Patel, G.K. Solanki, V.M. Pathak, *J. Electron. Mater.* 50 (2021) 5217–5225.
- [68] L. Lv, Z. Lin, T.D. Corrigan, J. Zhao, Z. Cao, L. Meng, C. Luan, Z. Wang, H. Chen, *J. Appl. Phys.* 109 (2011) 074512.
- [69] B. Şahin, H. Çetin, E. Ayyıldız, *Solid State Commun.* 135 (2005) 490–495.
- [70] J.H. Werner, *Appl. Phys. A* 47 (1988) 291–300.
- [71] M. Grajower, B. Desiatov, N. Mazurski, J. Shappir, J.B. Khurgin, U. Levy, *ACS Photonics* 4 (2017) 1015–1020.
- [72] A.A. Tarabsheh, M. Akmal, in: Proceedings to the 2019 6th International Conference on Electrical and Electronics Engineering (ICEEE), 2019, pp. 12–16.
- [73] M. Bashahu, P. Nkundabakura, *Sol. Energy* 81 (2007) 856–863.
- [74] Z. Ouennoughi, M. Chegaar, *Solid State Electron.* 43 (1999) 1985–1988.
- [75] A. Türüt, Turk. J. Phys. 44 (2020) 302–347.
- [76] P. Chattopadhyay, B. Raychaudhuri, *Solid State Electron.* 36 (1993) 605–610.
- [77] L. Calvet, R. Wheeler, M. Reed, *Appl. Phys. Lett.* 80 (2002) 1761–1763.
- [78] J.M. Ortega, W.C. Rheinboldt, *Iterative Solution of Nonlinear Equations in Several Variables*, SIAM, New York, 1970.
- [79] K. Ejderha, N. Yıldırım, A. Türüt, B. Abay, *Superlatt. Microstruct.* 47 (2010) 241–252.
- [80] D. Feiba, E. Bortoni, A. Oliveira, R. Rubinger, *Sol. Energy* 201 (2020) 420–436.
- [81] V.J. Chin, Z. Salam, K. Ishaque, *Appl. Energy* 154 (2015) 500–519.
- [82] S. Aazou, M.S. White, M. Kaltenbrunner, Z. Sekkat, D.A.M. Egbe, E.M. Assaid, *Energies* 15 (2022) 1667.
- [83] R.M. Corless, G.H. Gonnet, D.E. Hare, D.J. Jeffrey, D.E. Knuth, *Adv. Comput. Math.* 5 (1996) 329–359.
- [84] A. Ortiz-Conde, F.J.G. Sánchez, J. Muci, *Sol. Energy Mater. Sol. Cells* 90 (2006) 352–361.
- [85] C.H. Belgacem, A.A. El-Amine, *Silicon* 7 (2015) 279–282.
- [86] W. Jung, M. Guziewicz, *Mater. Sci. Eng. B-Adv.* 165 (2009) 57–59.
- [87] G.-P. Ru, R. Van Meirhaeghe, S. Forment, Y.-L. Jiang, X.-P. Qu, S. Zhu, B.-Z. Li, *Solid State Electron.* 49 (2005) 606–611.
- [88] P. Gammon, A. Pérez-Tomás, V. Shah, O. Vavasour, E. Donchev, J. Pang, M. Myronov, C.A. Fisher, M. Jennings, D.R. Leadley, *J. Appl. Phys.* 114 (2013) 223704.
- [89] H.K. Park, J. Choi, *Adv. Electron. Mater.* 4 (2018) 1700317.
- [90] S. Altindal Yerişkin, M. Balbaşı, S. Demirezen, *Indian J. Phys.* 91 (2017) 421–430.
- [91] J. Osvald, *Phys. Stat. Sol. A* 212 (2015) 2754–2758.
- [92] A. Grillo, A. Di Bartolomeo, *Adv. Electron. Mater.* 7 (2021) 2000979.
- [93] R.O. Ocaya, F. Yakuphanoglu, *Measurement* 186 (2021) 110105.
- [94] Z. Wang, S. Luo, J. Tan, K. Liu, P. Wangyang, S. Huanglong, T. Sun, X. Liu, Y. Deng, H. Li, *J. Electron. Mater.* 51 (2022) 2843–2855.
- [95] R.E. Walpole, R.H. Myers, S.L. Myers, K. Ye, *Probability and Statistics For Engineers and Scientists*, Macmillan, New York, 1993.
- [96] Y. Wang, S. Yang, D.R. Lambada, S. Shafique, *Sensor Actuat. A-Phys.* 314 (2020) 112232.
- [97] T. Yan, Z. Li, F. Cao, J. Chen, L. Wu, X. Fang, *Adv. Mater.* 34 (2022) 2201303.
- [98] P. Ji, S. Yang, Y. Wang, K. Li, Y. Wang, H. Suo, Y.T. Woldu, X. Wang, F. Wang, L. Zhang, Z. Jiang, *Microsyst. Nanoeng.* 8 (2022) 9.
- [99] Y. Liu, J. Guo, E. Zhu, L. Liao, S.-J. Lee, M. Ding, I. Shakir, V. Gambin, Y. Huang, X. Duan, *Nature* 557 (2018) 696–700.
- [100] K. Nassiri Nazif, A. Daus, J. Hong, N. Lee, S. Vaziri, A. Kumar, F. Nitta, M.E. Chen, S. Kananian, R. Islam, K.-H. Kim, J.-H. Park, A.S.Y. Poon, M.L. Brongersma, E. Pop, K.C. Saraswat, *Nat. Commun.* 12 (2021) 7034.
- [101] C.M. Went, J. Wong, P.R. Jahelka, M. Kelzenberg, S. Biswas, M.S. Hunt, A. Carbone, H.A. Atwater, *Sci. Adv.* 5 (2019) eaax6061.
- [102] P. Liao, X. Zhao, G. Li, Y. Shen, M. Wang, *Nanomicro Lett.* 10 (2018) 1–8.
- [103] Z. Xi, J. Ruan, C. Li, C. Zheng, Z. Wen, J. Dai, A. Li, D. Wu, *Nat. Commun.* 8 (2017) 15217.
- [104] B.-C. Min, K. Motohashi, C. Lodder, R. Jansen, *Nat. Mater.* 5 (2006) 817–822.
- [105] W. Huh, S. Jang, J.Y. Lee, D. Lee, J.M. Lee, H.-G. Park, J.C. Kim, H.Y. Jeong, G. Wang, C.-H. Lee, *Adv. Mater.* 30 (2018) 1801447.
- [106] X. Wei, X. Zhang, H. Yu, L. Gao, W. Tang, M. Hong, Z. Chen, Z. Kang, Z. Zhang, Y. Zhang, *Nan. Electron.* 7 (2024) 138–146.
- [107] X. Zhang, S. Chen, H. Ma, T. Sun, X. Cui, P. Huo, B. Man, C. Yang, *Nanomaterials* 14 (2024) 226.
- [108] J. Shi, J. Jie, W. Deng, G. Luo, X. Fang, Y. Xiao, Y. Zhang, X. Zhang, *Adv. Mater.* 34 (2022) 2200380.
- [109] S. Lee, A. Nathan, *Science* 354 (2016) 302–304.
- [110] R. Schmitzendorf, T. Kampen, W. Mönch, *J. Vac. Sci. Technol. B-Nanotechnol. Microelectron.* 15 (1997) 1221–1226.
- [111] B. Modi, J. Dhimmar, in: Proceedings to the 2012 1st International Conference on Emerging Technology Trends in Electronics, Communication & Networking, IEEE, 2012, pp. 1–6.
- [112] L.-F. Mao, *Pramana* 94 (2020) 16.
- [113] Y. Liu, Y. Liu, S. Qin, Y. Xu, R. Zhang, F. Wang, *Nano Res.* 10 (2017) 1880–1887.
- [114] B. Zhang, J. Liu, M. Ren, C. Wu, T.J. Moran, S. Zeng, S.E. Chavez, Z. Hou, Z. Li, A.M. LaChance, T.R. Jow, B.D. Huey, Y. Cao, L. Sun, *Adv. Mater.* 33 (2021) 2101374.
- [115] D. Wu, Y. Jiang, Y. Zhang, Y. Yu, Z. Zhu, X. Lan, F. Li, C. Wu, L. Wang, L. Luo, *J. Mater. Chem.* 22 (2012) 23272–23276.
- [116] V. Mikhelashvili, R. Padmanabhan, G. Eisenstein, *J. Appl. Phys.* 122 (2017) 034503.
- [117] G. Bhattacharya, A. Venimadhav, *J. Phys. D: Appl. Phys.* 55 (2022) 435101.
- [118] Y. Liu, P. Stradins, S.-H. Wei, *Sci. Adv.* 2 (2016) e1600069.

- [119] G. Myeong, W. Shin, K. Sung, S. Kim, H. Lim, B. Kim, T. Jin, J. Park, T. Lee, M.S. Fuhrer, K. Watanabe, T. Taniguchi, F. Liu, S. Cho, *Nat. Commun.* 13 (2022) 4328.
- [120] G. Milano, L. Boarino, C. Ricciardi, *Nanotechnology* 30 (2019) 244001.
- [121] W. Li, D. Jena, H.G. Xing, *J. Appl. Phys.* 131 (2022) 015702.
- [122] M. Hara, S. Asada, T. Maeda, T. Kimoto, *Appl. Phys. Express* 13 (2020) 041001.
- [123] Y.-J. Lin, *Appl. Phys. Lett.* 86 (2005) 122109.
- [124] C. Crowell, V. Rideout, *Solid State Electron.* 12 (1969) 89–105.
- [125] M. Hara, H. Tanaka, M. Kaneko, T. Kimoto, *Appl. Phys. Lett.* 120 (2022) 172103.
- [126] J. Appenzeller, M. Radosavljevic, J. Knobch, P. Avouris, *Phys. Rev. Lett.* 92 (2004) 048301.
- [127] L. Lv, J. Yu, M. Hu, S. Yin, F. Zhuge, Y. Ma, T. Zhai, *Nanoscale* 13 (2021) 6713–6751.
- [128] R.A. Vega, *IEEE Trans. Electron Devices* 53 (2006) 1593–1600.
- [129] L. Wu, A. Wang, J. Shi, J. Yan, Z. Zhou, C. Bian, J. Ma, R. Ma, H. Liu, J. Chen, Y. Huang, W. Zhou, L. Bao, M. Ouyang, S.J. Pennycook, S.T. Pantelides, H.-J. Gao, *Nat. Nanotechnol.* 16 (2021) 882–887.
- [130] J. Di, J. Du, Z. Lin, S. Liu, J. Ouyang, J. Chang, *InfoMat* 3 (2021) 293–315.
- [131] I. Missoum, Y. Ocak, M. Benhaliliba, C. Benouis, A. Chaker, *Synth. Met.* 214 (2016) 76–81.
- [132] Ö. Güllü, Ş. Aydoğán, A. Türüt, *Microelectron. Eng.* 85 (2008) 1647–1651.
- [133] W. Hu, T. Wang, J. Yang, *J. Mater. Chem. C* 3 (2015) 4756–4761.